Petrogenesis of Mesozoic Li-, Cs-, and Ta-rich (LCT) pegmatites from the Neoproterozoic Jiangnan Orogenic Belt, South China: An alternative origin model for the LCT type pegmatite

Jian-Feng Chen [a,b,c], Chun-Hua Wen [b], Zheng-Hang Lv [d,e,*], Jian-Zhong Huang [b], Jin-Xu Zhang [b], Yong Tang [d], Yun Du [b], Chuang-Hua Cao [b]

[a] Geophysical and Geochemical Survey Institute of Hunan, Changsha 410116, PR China
[b] Hunan Institute of Geological Survey, Changsha 410116, PR China
[c] Key Laboratory of Metallogenic Prediction of Nonferrous Metals and Geological Environment Monitoring, Ministry of Education, Central South University, Changsha 410083, PR China
[d] Institute of Geochemistry, Chinese Academy of Sciences, Guiyang 55081, PR China
[e] Key Laboratory of Critical Minerals Metallogeny in University of Yunnan Province, School of Earth Sciences, Yunnan University, Kunming 650500, PR China

ARTICLE INFO

ABSTRACT

According to the classical petrogenesis model, Li-, Cs-, and Ta-rich (LCT) pegmatites juxtaposed in the same regional zonation are generally formed by unidirectional successive crystallization differentiation of the common parental granitic melt. However, this model cannot explain the origin of the Mesozoic LCT pegmatites from the East Jiangnan Orogenic Belt (JOB), South China. Herein, we studied the geology, zircon U–Pb ages, Hf isotope compositions, monazite U–Th–Pb ages, and Nd isotope compositions of three types of pegmatites in Renli, East JOB, South China to reveal their petrogenesis. The Renli pegmatites distributed in or around the Mufushan batholith, show mineralization zoning with distance from the batholith. The studied pegmatites were formed at the Early Cretaceous, with a decreasing trend from ca. 141 Ma for two-mica microcline pegmatite (type I) to 134 Ma for muscovite–albite–spodumene pegmatite (type III). The Renli pegmatites have coupled Hf–Nd isotope compositions and consistent Hf isotope compositions with the Mufushan granites. From the spatial–temporal, source and differentiation relationships between the Renli pegmatites and the Mufushan granites, we propose that type I pegmatites originates from biotite monzogranite while type II (muscovite–microcline–albite pegmatite) and type III pegmatites originate from the two-mica monzogranite and muscovite monzogranite, respectively, indicating a new model of parallel differentiations of triple granitic melts for the origin of LCT pegmatites in South China. The Renli pegmatites have a similar Hf isotope composition to the Neoproterozoic granitoids and the backarc sedimentary rocks of the Lengjiaxi Group formed during the Jiangnan orogeny. Combining with previous studies, we suggest that the Mesozoic Renli LCT pegmatites originated from reworking materials of the Neoproterozoic JOB caused by slab roll back of the paleo-Pacific Ocean plate during subduction.

1. Introduction

Granitic pegmatites (hereinafter referred to as pegmatites) have garnered immense attention because of their rare-earth element enrichment namely Li, Be, Nb, Ta, and Cs, which are listed as strategic mineral sources by many countries. Although the favorable tectonic settings of pegmatites still remain under debate, the Li-, Cs-, Ta-rich (LCT) pegmatites appear dominantly in convergent orogenic belts and correlate with orogenic, especially postorogenic, magmatisms (Černý,

1991; Černý et al., 2012) and supercontinent assembly temporally (e.g., McCauley and Bradley, 2014; Tkachev, 2011). In China, LCT pegmatites are widely exposed in the Altai, East Tianshan, West Kunlun, and Songpan–Ganzi Orogenic Belts, and most of them have been proposed to form in a postorogenic extension stage after accretion or collision orogeny (e.g., Lv et al., 2012, 2021a; Li et al., 2020a; Fei et al., 2020; Wang et al., 2020; Yan et al., 2022).

The Jiangnan Orogenic Belt (JOB), South China, is a convergence zone formed by Yangtze and Cathaysia block collision during the

---

Neoproterozoic (e.g.,Wang et al., 2014a, 2017; Zhou et al., 2009). Thus far, two periods of rare-metal pegmatites have been verified in the JOB. The early-one is represented by the Neoproterozoic pegmatite exposed only in the Fanjingshan area, West JOB. It comprises tens of pegmatites with limited Nb–Ta–Sn mineralization, which genetically relates to the Fanjingshan muscovite granite, and is formed by the partial melting of sedimentary rocks and high degrees of fractional crystallization of granitic melts after continental collision at ca. 830 Ma (Lv et al., 2021a). The late one is comprises of>1000 pegmatites distributed in or around the Yanshanian Mufushan batholith (YMB), East JOB. Recent exploration reveals that plenty of pegmatites have large potential for rare-metal (Nb–Ta ± Li ± Be) mineralizations, especially those exposed in the Renli mining area, South YMB (Zhou et al., 2019a, b) (Fig. 1). The YMB mainly comprises granodiorite, biotite monzogranite (BMG), and two-mica monzogranite (TMG) (Wang et al., 2014b), and the highly fractionated granitic phase, such as muscovite granite, is almost absent. In addition, lots of the pegmatites are widely distributed in the granodiorite, BMG and TMG (Fig. 1), and they have distinct mineral assemblages and mineralizations. These granite-hosted pegmatites also differ to those emplaced in sedimentary rocks. According to the classical model, a successive and (sub)vertical fractionation sequence of a granitic melt, normally featured by a lower biotite granite, an intermediate two-mica granite, and an upper muscovite granite, is essential for pegmatite regional zonation generation, and the most fractionated granite phase is

directly responsible for all types of pegmatites in the same zonation (e. g., Černý, 1991; London, 2018). Moreover, pegmatites derived from the upper fractionated granitic melt are impossible to emplace in the lower granitic phase. Therefore, the classical model is hard to explain the pervasive occurrence of pegmatites in various granitoids. Were they originated from a common granitic source or multiple sources, still remains unanswered?

Although some studies have been conducted on the granites and adjacent pegmatites in the Mufushan area, especially the geochronology (Li et al., 2019, 2020b; Xiong et al., 2020; Zhou et al 2020), mineralizing mechanism (Liu et al., 2019; Zhou et al., 2019a), and magma ecolution (Wang et al., 2019; Yang et al., 2019; Zhou et al., 2019b) studies of the Renli No.5 pegmatite, which is the most remarkable Nb–Ta mineralization dike in the Mufushan area, it is not enough to reveal the petrogenesis of various pegmatites, especially the relationship between pegmatites and granitoids. Herein, monazite and zircon U–(Th)–Pb chronology was used to study the formation ages of the three types of pegmatites, including the Nos. 7, 2, 3, and 47 pegmatites, distributed in the Renli mining area, South YMB, and Nd–Hf isotope compositions to determine their source, aiming to decipher the petrogenesis of LCT pegmatite that formed in the JOB, South China.
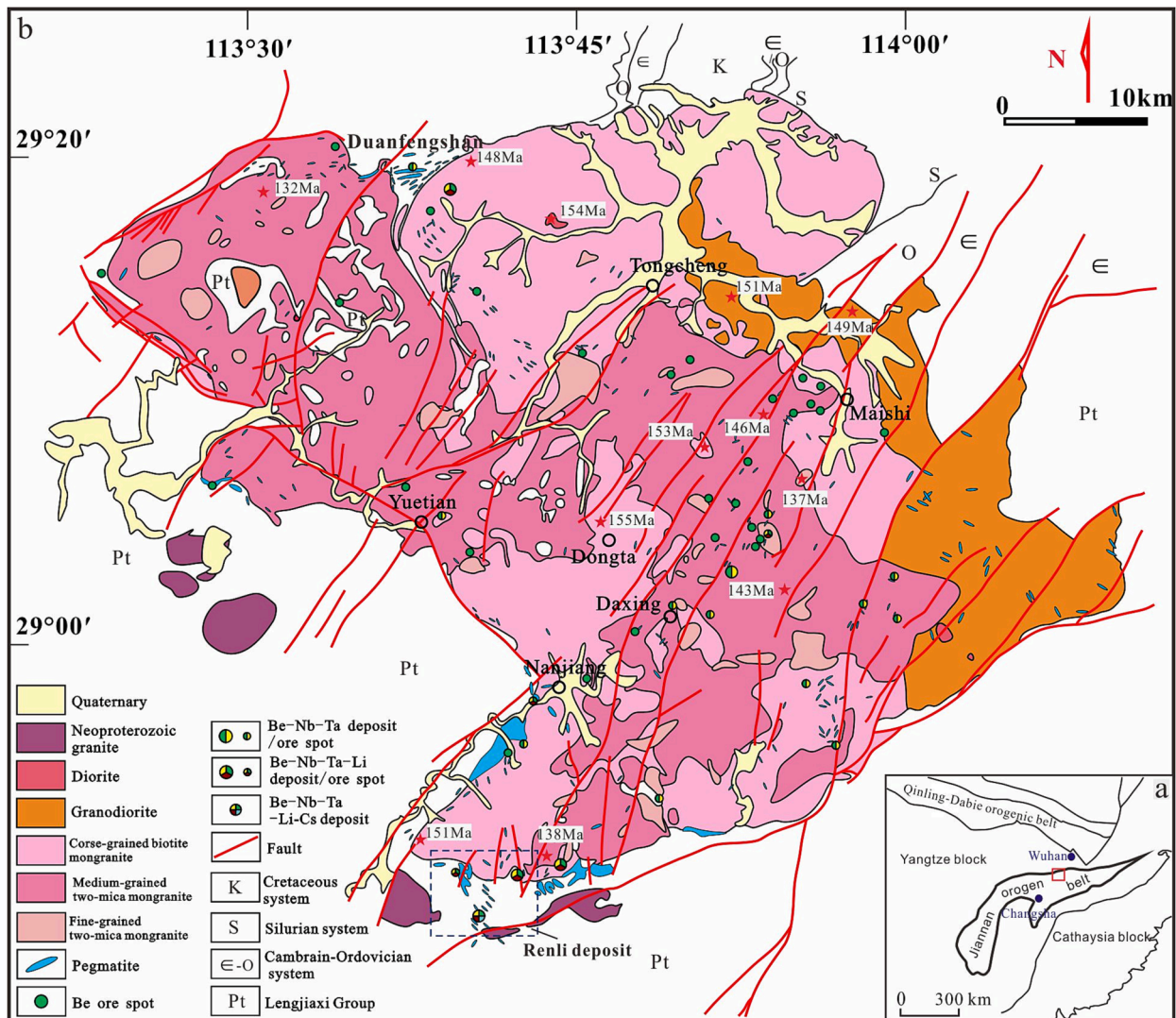

Fig. 1. Tectonic outline of the JiangnanOrogen Belt(a) and the geological sketch map of the Mufushan area (b) (modified from Li et al., 2021).

2. Geological setting

The Renli pegmatite-type rare-metal deposit is located in the Mufushan region, the central–eastern segment of the JOB in South China (Fig. 1a). The JOB, also referred to as the Jiangnan Orogen, Jiangnan paleocontinent, Jiangnan block, and Jiangnan fold belt (Cawood et al., 2013;Shu et al., 1994; Wang et al., 2006; Xu et al., 2017;Yao et al., 2014; Yu et al., 2021), was formed by the Neoproterozoic amalgamation of the Yangtze and Cathaysia blocks due to the subduction and collision processes before ca. 820 Ma (Li, 2006; Li et al., 2009; Shan et al., 2017; Wang et al., 2014a; Zhao et al., 2011) and reactivated at ~ 130 Ma because of the paleo-Pacific plate subduction toward the Eurasic plate (Shu and Zhou, 2002; Wang and Zhou, 2002; Wang and Shu, 2012). The central–eastern JOB is an important polymetallic metallogenic belt in South China and hosts large amounts of Au, Sb, W, Cu, Co, Pb, Zn, and even Be, Nb, and Ta ore deposits/spots(Deng et al., 2017; Hu and Peng, 2018; Lv et al., 2021a; Wang et al., 2017a; Wen et al., 2021; Xiong et al., 2020; Xu et al., 2017; Zhou et al., 2019b; Zou et al., 2018).

The Mufushan complex massif, located at the junction of Hunan, Hubei, and Jiangxi Provinces with an exposure area of>2000 km^2, is composed of the extensive Yanshanian granitoid batholith (ca.158–138 Ma) (Ji et al., 2017, 2018; Li, 2017, Li et al., 2020b; Wang et al., 2014b; Xu et al., 2019a,b; Xiong et al., 2020) and local Neoproterozoic granitic stocks (ca. 838–816 Ma) (HIGS, 2009; Shan et al., 2017) in the western and southwestern regions (Fig. 1).The YMB comprises several periods of intrusions (Fig. 1), including diorite(154 Ma,Wang et al., 2014b), granodiorite (151–149 Ma; Ji et al., 2018; Wang et al., 2014b), BMG (155–148 Ma; HIGS, 2009; Ji et al., 2017, 2018; Li et al., 2017; Wang et al., 2014b; Xiong et al., 2020), medium-grained TMG (146–138 Ma, Ji et al., 2017; Li et al., 2020b; Wang et al., 2014b), and fine-grained TMG (137 Ma; HIGS, 2009), with a decreasing trend in age from the reported zircon U–Pb ages.

Exposed as strata around the YMB (except northeast) or as fragmentation isolated in the batholith is the Lengjiaxi Group of the Neoproterozoic Qingbaikou system, which is ~ 6,700–10,127 m thick comprising sericitized slate, carbonaceous sericite silty slate, graywacke, and schist (Gao et al., 2011; Yang et al., 2020); schist occurs in the exocontact zone of the YMB within 0–6 km. Moreover, the lower Paleozoic Cambrian, Ordovician, and Silurian systems are found in the northeast.

Several ore deposits distributed around the YMB can be found, namely, the Taolin and Lishan large-scale Pb–Zn–fluorite deposits (Ding and Rees, 1984; Shan et al., 2017; Yu et al., 2021) and Duanfengshan and Renli Nb–Ta–(Li) rare-metal deposits. The latter two are the newly discovered, large-superlarge scale rare-metal deposits situated in the north and south of Mufushan batholiths, respectively(Li et al., 2017; Li et al., 2018; Li et al., 2020a; Li et al., 2021; Wei et al., 2021; Zhou et al., 2019b). Moreover, high amounts of rare-metal (Be, Nb, and Ta) pegmatites (Fig. 1) were found in the exocontact zone of the YMB.

3. Ore deposit geology

Located within the contact zone between the southern YMB and Lengjiaxi metasedimentary strata, the Renli rare metal ore deposit (Fig. 2) is the largest known granitic pegmatite rare-metal deposit with high-grade Ta and Nb (10791 t of Ta$_2$O$_5$, average grade at 0.036 wt%;
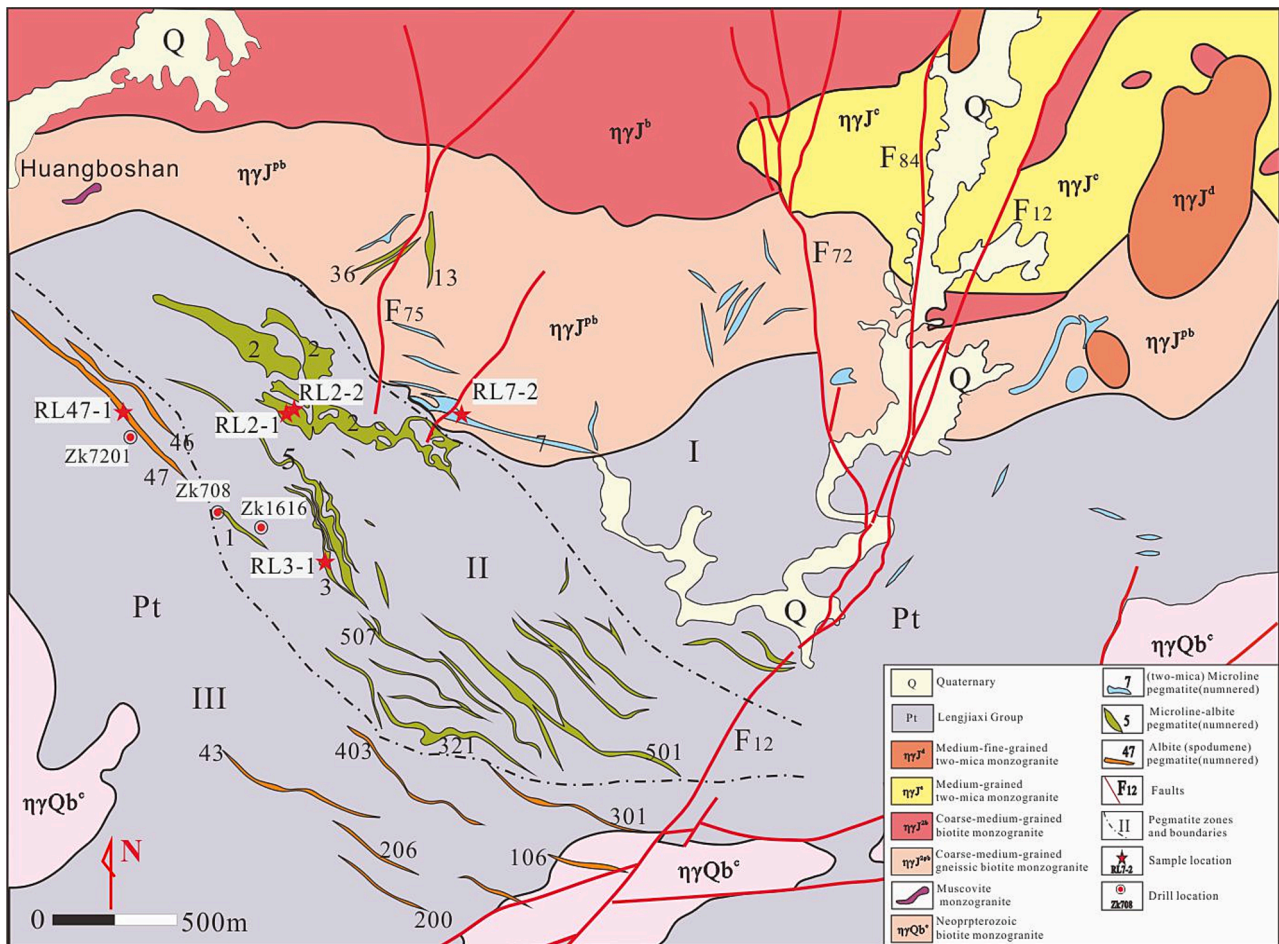

Fig. 2. Geological map of the Renli rare-metal deposit (modified from Li, 2017). Pegmatite spatial zonation: type I–microcline pegmatite; type II–microcline-albite pegmatite; and type III–albite pegmatite.

14057 t of Nb$_2$O$_5$, average grade at 0.047 wt%; Zhou et al., 2019b). The exposed strata in the south of the mining area belongs to the Neoproterozoic Lengjiaxi Group (Fig. 2) and comprises garnet-bearing two-mica schist, sericite schist, and banded slate, with NW-trending and NW-dipping (dip angles 20–50°). The fault structures in the mining area are mainly NE-oriented, with a smaller number of NNE-oriented faults, which cut the metasedimentary rocks, granites, and pegmatites (Li et al., 2020a,b, Li et al., 2021; Xiong et al., 2020).

Neoproterozoic and Yanshanian granitic intrusive rocks are extensively exposed in the Renli mining area (Fig. 2). The former is medium- to fine-grained and weakly gneissic biotite plagioclase granite that

occurs in the southwestern and southern regions of the district. The latter is composed of (1) coarse- to medium-grained BMG occurring in the north with a gneissoid margin, (2) medium- and fine-grained TMG occurring in the northeast, (3) a small amount of fine- to medium-grained muscovite monzogranite (MMG) dikes, and (4) plenty of pegmatite dikes/veins. Precious zircon U–Pb age analysis shows that the granites exposed in the Renli district have consistent zircon U–Pb ages of 140–138 Ma (Li et al., 2020b; Xiong et al., 2020) while the BMG samples obtained from the drillings of ZK708, ZK1616, and ZK7201 (locations in Fig. 2) show an older age of ca.146 Ma (Li et al., 2017).

Several hundreds of pegmatite dikes are found in the Renli mining
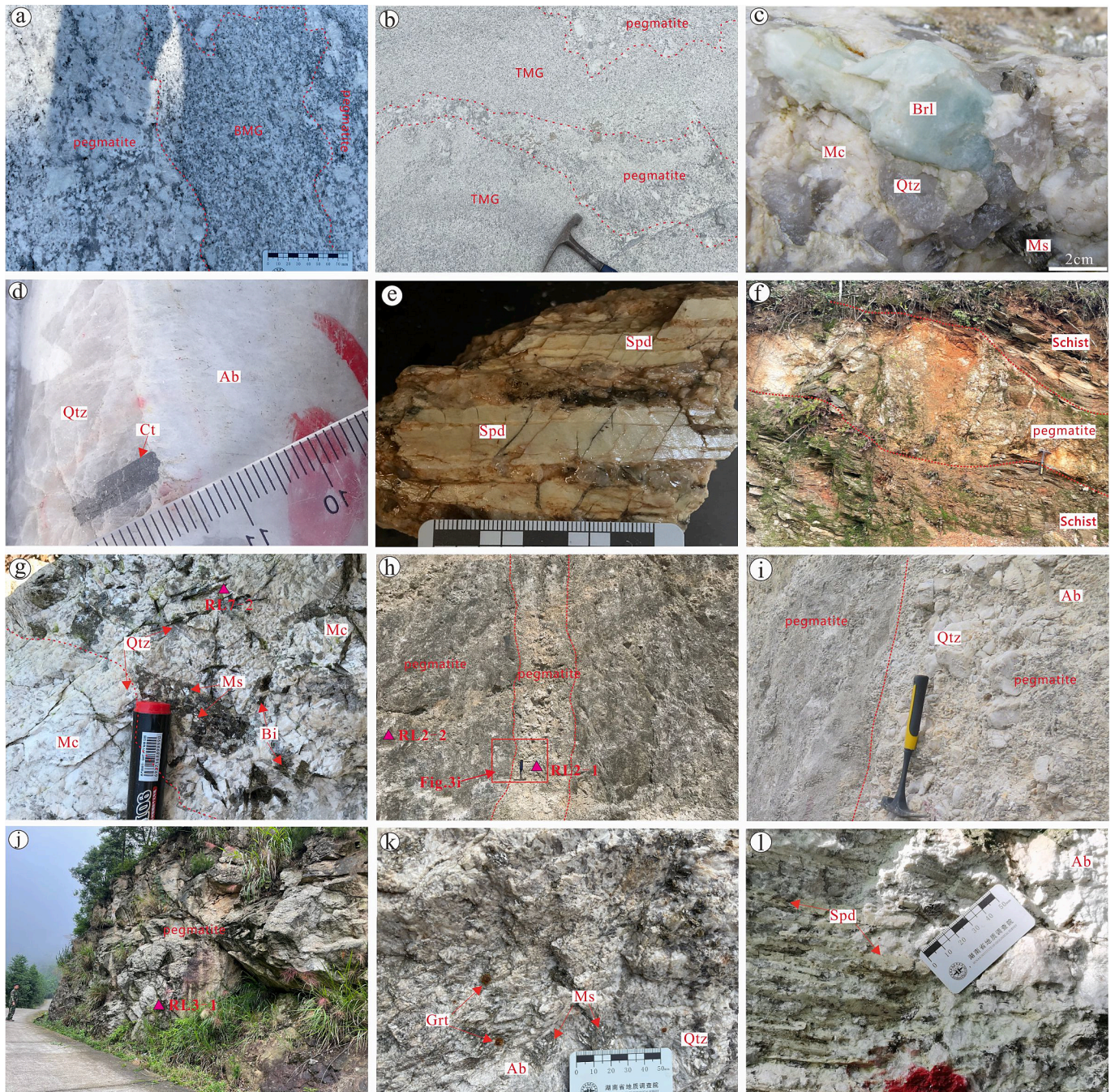
Fig. 3. Field photographs of pegmatites in the Renli mining area. Outcrop of type I pegmatites in BMG (a); outcrop of type II pegmatites in TMG (b); beryl-bearing pegmatite (c); coltan-bearing pegmatite samples (d); spodumene-bearing pegmatite(e); outcrop of spodumene–albite pegmatite of the No.47 (f); outcrop of two mica-microcline pegmatite of the No.7 pegmatite (g); outcrop of microcline–albite pegmatite of the No.2 pegmatite (h, i) and the later pegmatite intrusion (h); outcrop of microcline–albite pegmatite of the No.3 pegmatite (j, k); spodumene–albite pegmatite of the No.47 (l). Ab = albite; Brl = Beryl; Bi = Biotite; Mc = microcline; Ms = Muscovite; Qtz = quartz; Grt = Garnet; Spd = spodumene.

area. About 140 dikes have large sizes (width > 1 m): 95 hosted in the YMB and 45 dikes emplaced in the Lengjiaxi Group as an intrusion. The pegmatites show diverse mineral assemblages and mineralizations with distance from the YMB. Almost all the pegmatite dikes hosted in the BMG belong to biotite–muscovite–microcline pegmatite (type I) (Fig. 3a) and basically lack rare-metal minerals, but occasionally some beryl or small needle-like coltan. The pegmatites in the TMG belong to muscovite–microcline–albite pegmatite (type II) (Fig. 3b), and contain a certain amount of beryl (Fig. 3c) and coltan (Fig. 3d). These pegmatites emplaced in granites generally exhibit irregular shapes, unconstant strikes and limited scales. There are two classifications of pegmatite dikes in the Lengjiaxi Group (Fig. 3f). The first is muscovite–microcline–albite pegmatite (type II) and locates in an ~ 1–1.7 km-wide contact zone between the YMB and schist (Fig. 2). It is featured by significant Nb and Ta mineralizations, such as Nos. 2, 3, and 5 pegmatite dikes, containing 15 %, 13 %, and 58 % of the total Ta_2O_5 and 17 %, 13 %, and 53 % of the total Nb_2O_5 in the Renli Nb–Ta ore deposit, respectively. Coltan is the main rare-metal mineral and appears as needle-like or euhedral tabular crystals, with 0.1–1.5 cm grain sizes and intergrowth with quartz and albite (Fig. 3d and 4c). The second classification is muscovite–albite–spodumene pegmatite (type III), which locates in the southern and southwestern parts of the mining area and is identified by the presence of spodumene (Fig. 3e and 4d, e) and few lepidolite (Fig. 4e) and less coltan (Fig. 4f) compared to type II. With distance from the batholith, the dominant alkaline elements of pegmatite change from K to K + Na and then to Na(+Li), and the rare-metal mineralization type changes from Be to (Be +)Nb + Ta and then to (Be +)Nb + Ta + Li. The above geology and mineralization characteristics indicate the Li–Cs–Ta (LCT) affinity of the Renli pegmatites.

4. Sampling

Zircon separation, U–Pb dating, and Hf isotope analysis, were performed on the RL7-2, RL2-2, and RL47-1 samples collected from Nos. 7, 2, and 47 pegmatites, respectively (Fig. 2). Monazite separation, U–Pb dating, and Nd isotope analysis were performed on the RL2-1, RL2-2,

and RL3-1 collected from Nos. 2, and 3 pegmatites, respectively (Fig. 2).

4.1. RL7-2

RL7-2 was collected from No.7 pegmatite, which is the largest type I pegmatite in the Renli mining area. The outcrop of the No. 7 pegmatite is 2000-m long and 80–140-m wide, with a strike and dip angles of 330°–350° and 50°–80°, respectively. The pegmatite has simple internal zonation, i.e., a graphic pegmatite zone, a biotite–muscovite–microcline–quartz zone, and a locally developed blocky microcline zone. RL7-2 was collected from the biotite-muscovite-microcline-quartz zone with a composition of 60 % microcline, 25 % quartz, 10 % muscovite, and 4 % biotite (Fig. 3g).

4.2. RL2-1 and RL2-2

RL2-1 and RL2-2 were collected from No.2 pegmatite, which is the largest type II pegmatite in the Renli mining area. It shows three large outcrops with average length of 2900 m and width of 50 m. The largest outcrop of the pegmatite shows a complex shape featuring branch and recombination, with strike and dip angles of 310°–330° and 25°–40°, respectively. and was intrusion of a late small pegmatite vein with a sharp contact (Fig. 3h, i). The No.2 pegmatite is almost homogeneous in mineralogy and texture with no evident internal zonation. For comparison, the later intrusion vein is uneven in mineral proportion and size. RL2-2 was collected from the foot wall of the No. 2 pegmatite (Fig. 3h) and has a composition of 25 % microcline, 35 % albite, 30 % quartz, and 8 % muscovite (Fig. 4a, b). RL2-1 was collected from the later pegmatite intrusion in the No. 2 pegmatite (Fig. 3h) and has a composition of 10 % microcline, 35 % albite, 40 % quartz, and 12 % muscovite and is identified by remarkable Nb–Ta mineralization.

4.3. RL3-1

RL3-1 was collected from the No. 3 pegmatite (Fig. 3j), which also belongs to the type II pematite. It is located near the No. 5 pegmatite
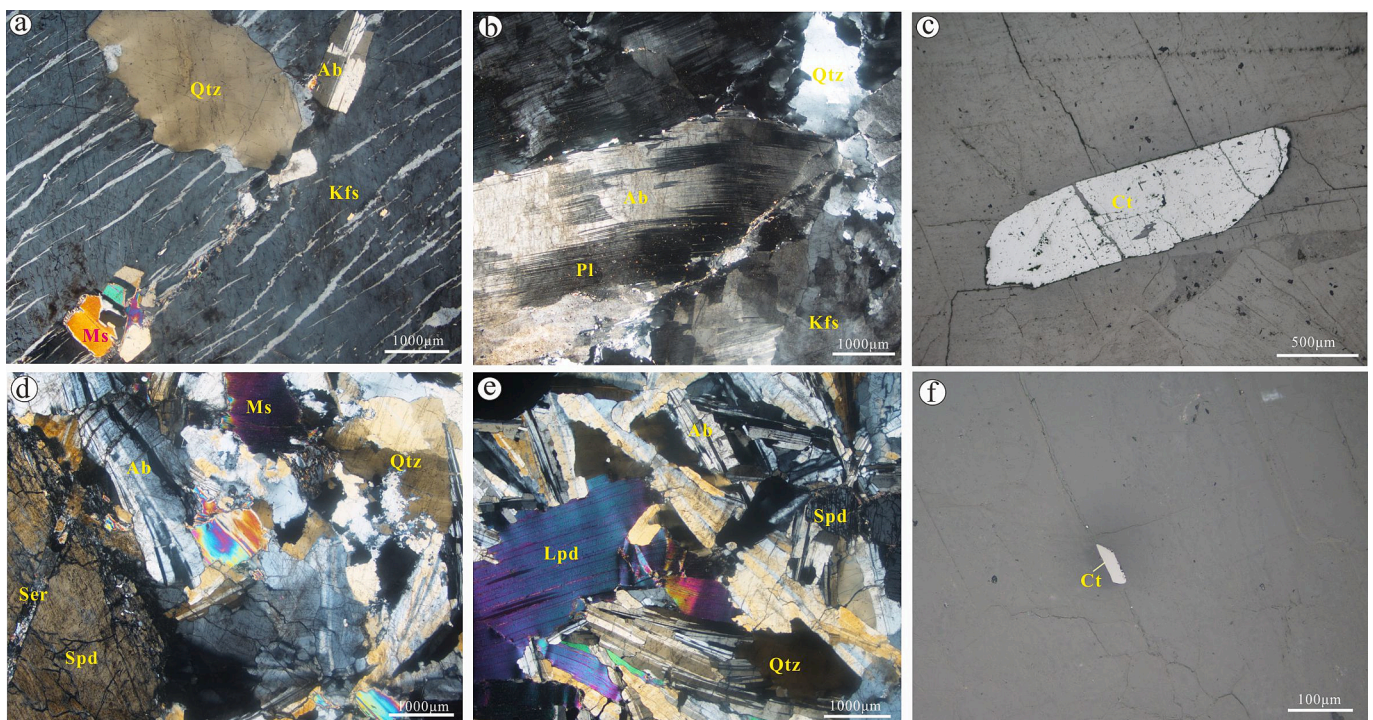

Fig. 4. Photomicrographs of pegmatite samples from the Renli deposit. muscovite–microcline–albite pegmatite (type II) (a, b); euhedral coltan in type II pegmatite (c); muscovite–albite–spodumene pegmatite (type III) (d, e); euhedral coltan in type III pegmatite (f).

(Fig. 2) featured by large-scale Nb–Ta mineralization. It shows a tabular shape in outcrop (Fig. 3j) and has a length of 1280 m and a width of 2–6 m, with general strike and dip angles of 280°–310° and 25°–35°, respectively. The No. 3 pegmatite also shows simple mineralogy and internal zonation including only a graphic zone and a muscovite–quartz–albite zone. RL3-1 was collected from the muscovite–quartz–albite zone and is composed of 10 % microcline, 40 % albite, 30 % quartz, and 18 % muscovite (Fig. 3k). Coltan is the dominant ore-forming mineral (Fig. 4c).

4.4. RL47-1

RL47-1 was collected from the No.47 pegmatite (Fig. 3f), which is the largest spodumene-rich pegmatite of the type III pegmatite exposed in the Renli mining area. The pegmatite is located in the western part of the Renli mining area and intruded into the schist of the Lengjiaxi Group (Fig. 2). It is ca.2000-m long and 1.5–7.0-m wide with a strike of NNW 300–310° and a dip angle of 25–35°. The No.47 pegmatite also shows simple internal zonation that mainly comprises an albite–spodumene zone and a muscovite-quartz zone. The RL47-1 sample was collected from the albite–spodumene zone with rock-forming minerals of 40 % albite, 30 % spodumene, 20 % quartz, and 8 % muscovite (Fig. 3l).

5. Analytical methods

All preparatory and analytical works were performed at the State Key Laboratory of Ore Deposit Geochemistry (SKLODG), Institute of Geochemistry, Chinese Academy of Sciences. The work details are as follows.

5.1. Zircon U–Pb dating and Hf isotope analysis

Zircons were separated from the pegmatites using conventional density and magnetic separation techniques and then hand-picked under a binocular microscope. Zircons were mounted onto epoxy and polished to about half their thickness. Transmitted and reflected light microscopy and cathodoluminescence (CL) imaging were performed on the zircons to reveal their internal structure (Fig. 5).

Zircon U–Pb dating was performed using laser ablation inductively coupled plasma mass spectrometry (LA–ICP–MS; GeoLasPro laser ablation system) coupled with an Agilent 7700ICP-MS system. A 193-nm ArF excimer laser, homogenized by a set of beam delivery systems, was focused on a zircon surface with 10 J/cm^2 flux under conditions of 32 µm spot size, 30 kV accelerating voltage, and 5 Hz repetition rate for 40 s. Helium was used as a carrier gas to transport the aerosol to the ICP–MS system. Zircon 91,500 was used as an external standard for the correction of instrumental mass discrimination and elemental fractionation (Wiedenbeck et al., 1995). Zircon GJ-1 and Plešovice were treated as quality control references for geochronology. Zircon common Pb concentration was externally calibrated against NIST SRM 610 with Si as an internal standard, whereas Zr served as the internal standard for the other trace elements (Hu et al., 2011; Liu et al., 2010a). Data reduction was performed offline with ICPMSDataCal (Liu et al., 2010b).

Hf isotope compositions were subsequently obtained from the same zircon spots previously analyzed for U–Pb dating, as guided by CL images. Zircon Hf isotopic analyses were performed using a Nu Plasma high resolution multiple-collector (MC)-ICP-MS (Nu Instruments ltd., UK) equipped with a GeoLas 2005 193 nm ArF excimer laser ablation system at the SKLODG, GIGCAS under conditions of 60 µm spot size, 10 Hz repetition rate, 15–20 J/cm^2 energy density, and He carrier gas. Raw count rates for ^{172}Yb, ^{173}Yb, ^{175}Lu, ^{176}(Hf + Yb + Lu), ^{177}Hf, ^{178}Hf, ^{179}Hf, and ^{180}Hf were collected simultaneously. The correction of the isobaric interference of ^{176}Lu on ^{176}Hf was done by measuring the intensity of an interference-free ^{175}Lu isotope, and ^{176}Lu/^{177}Hf ratios were calculated using a recommended ^{176}Lu/^{175}Lu ratio of 0.02669. Similarly, correction of the interference of ^{176}Yb on ^{176}Hf was done by measuring an interference-free ^{172}Yb isotope, and ^{176}Hf/^{177}Hf ratios were calculated using a ^{176}Lu/^{172}Yb ratio of 0.5886 (Chu et al., 2002).
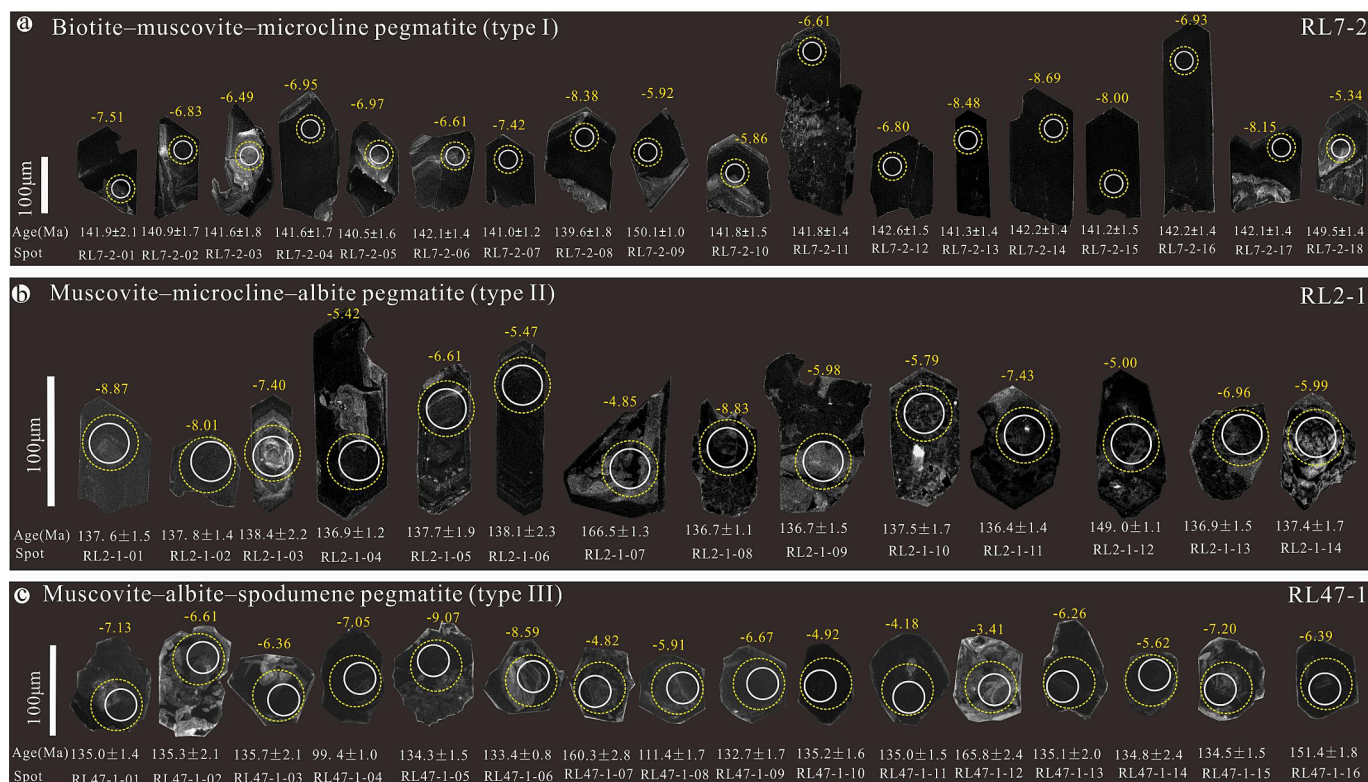

Fig. 5. Cathodoluminescence (CL) images of zircons from the Renli pegmatite. White and yellow circles indicate the laser spots of U–Pb dating and Hf isotope analysis, respectively.

The correction of time-dependent drifts of Lu–Hf isotopic ratios was performed via linear interpolation based on the variations of 91,500 and Penglai. For data quality evaluation, 91,500 and GJ-1 were reanalyzed as unknowns. The obtained $^{176}Hf/^{177}Hf$ ratios were 0.282295 ± 0.000027 (n = 14, 2σ) for 91,500 and 0.282904 ± 0.000006 (n = 30, 2σ) for Penglai, which is in good agreement with the recommended $^{176}Hf/^{177}Hf$ ratios within 2σ (0.282307 ± 58 and 0.282906 ± 0.000010; Griffin et al., 2006; Li et al., 2010).

A decay constant for ^{176}Lu of $1.865 \times 10^{-11}a^{-1}$ (Scherer et al., 2001) and chondritic ratios of $^{176}Hf/^{177}Hf = 0.282772$ and $^{176}Lu/^{177}Hf = 0.0332$ (Blichert-Toft and Albarède, 1997) were adopted for the calculation of the initial $^{176}Hf/^{177}Hf$ and $\varepsilon_{Hf}(t)$ values. Depleted mantle Hf model ages (T_{DM}) were calculated from the measured $^{176}Lu/^{177}Hf$ and $^{176}Hf/^{177}Hf$ ratios of the zircons, assuming a present $^{176}Hf/^{177}Hf$ ratio of 0.283250 and a $^{176}Lu/^{177}Hf$ ratio of 0.0384 for the depleted mantle (Griffin et al., 2002). The average crustal $^{176}Lu/^{177}Hf$ value of 0.015 was adopted for the calculation of the two stage model ages (Griffin et al., 2002).

5.2. Monazite U–Pb dating and Nd isotope analyses

Monazite U–Th–Pb dating was done by LA-ICP-MS. Laser sampling was performed using a GeolasPro LA system comprising a COMPexPro 102ArF excimer laser (193 nm wavelength and 200 mJ maximum energy) and a MicroLas optical system. ICP–MS (Agilent 7700e ICP–MS instrument) was performed for acquiring ion-signal intensities. Helium was used as the carrier gas and argon was used as the make-up gas; both were mixed using a *T*-connector before they were entered into the ICP–MS instrument. A "wire" signal smoothing device was included in this LA system through which smooth signals are produced even at very low laser rates down to 1 Hz (Hu et al., 2008). The spot size of the laser was set to 24 μm, and the frequency of the laser was 5 Hz. Monazite standard Harvard 117,531 (272 ± 2 Ma; Tomascak et al., 1996) and glass NIST610 were used as external standards for U–Th–Pb dating and trace element calibration, respectively. The pegmatite monazite standards Coqueiro and Paraíso (Goncalves et al., 2016) were used as a secondary standard to monitor data quality. Each analysis incorporated a background acquisition of ~ 20–30 s followed by 50 s of data acquisition from the sample. The Excel-based software ICPMSDataCal was used to perform offline selection and integration of background and analyzed signals, time-drift correction, and quantitative calibration for trace element analysis and U–Th–Pb dating. Concordia diagrams were constructed, and Isoplot 4.15 was used to performed weighted mean calculations (Ludwig, 2011).

In situ monazite Nd isotope measurements were conducted using a Nu Plasma III MC–ICP–MS (Nu Instruments) that was attached to a RESOlution-155 ArF 193 nm laser ablation system (Australian Scientific Instruments). Monazite was ablated in a mixture of helium (350 mL/min) and nitrogen (2 mL/min) atmospheres at 30 s baseline time, 40 s ablation time, 60 μm spot size, 6 Hz repetition rate, and 6 J/cm² energy density. The interference of ^{144}Sm on ^{144}Nd was derived from the ^{147}Sm intensity using a natural $^{144}Sm/^{147}Sm$ ratio of 0.205484 (Isnard et al., 2005). The mass bias factor of Sm with a true value of 1.08680 was calculated from the measured isotopic ratio of $^{147}Sm/^{149}Sm$ (Isnard et al., 2005). The mass bias of $^{143}Nd/^{144}Nd$ was normalized to $^{146}Nd/^{144}Nd$ of 0.7129 with an exponential law. One apatite standard Durango every-five samples and other two apatite standards (AP1 and MAD) every 30 unknown samples were treated as quality control. The measured $^{143}Nd/^{144}Nd$ ratio for the apatite standard AP1 was 0.512342 ± 0.000014 (n = 12), near the recommended value (AP1: 0.512352 ± 0.000024) (Yang et al., 2014).

6. Analytical results

6.1. CL and Th–U features of zircon samples

For the RL7-2 sample, the zircons are euhedral (Fig. 5a) and transparent or translucent. Zircons lengths are from 100 to 300 μm, with length/width ratios of 2:1–4:1. Most zircons exhibit weak oscillatory growth zoning, and a few of them are almost black (grains 12–16) in their CL images (Fig. 5a). Their Th and U contents are in the ranges of 82–620 and 5154–21886 ppm, respectively, with consistent Th/U ratios of 0.02–0.03 (Table 1).

For the RL2-2 sample, the zircons are euhedral to subhedral and translucent and 80–120-μm long, with length/width ratios of 1:1 to 3:1 (Fig. 5b). Some zircons exhibit weak (grains 1, and 2) to clear (grains 3, 4, 5, 6, and 9) oscillatory growth zoning, and some (grains 7, 10, 11, 12, 13, and 14) show a blurred and spongy inner core and weak oscillatory growth zoning in outer rims. Their Th and U contents are 293–3749 and 4292 to 45588 ppm, respectively, with Th/U ratios of 0.02–0.09 (Table 1).

For the RL47-1 sample, the zircons are subhedral and translucent, with crystal sizes 70–110-μm long, with length/width ratios of 1:1–1.5:1. All the zircon grains exhibit irregular and weak oscillatory growth zoning (Fig. 5c). Their Th and U contents are 235 –30401 and 4012–74993 ppm, respectively, with Th/U ratios of 0.03–0.41 (Table 1).

6.2. CL and Th–U features of monazite samples

The monazites from the RL2-1, RL2-2, and RL3-1 samples exhibit almost the same feature, as shown in the CL images (Fig. 6a, b, c); they are euhedral to subhedral, 80–130-μm long, and 40–100-μm wide with low length/width ratios. In addition, most of the grains lack oscillatory growth zoning in their CL images. They contain high Th (118,000–266,000 ppm) and U (18,000–83,000 ppm) contents and relatively low Pb (1200–3000 ppm) contents (Table 2).

6.3. Zircon U–Pb ages

For the RL7-2 sample of microcline pegmatite, U–Pb age determination was performed on 18 zircons (Fig. 5a). Nos. 9 and 18 grains yielded old $^{206}Pb/^{238}U$ ages of 150.1 ± 1.0 and 149.5 ± 1.4 Ma, respectively, indicating the occurrence of zircon xenocryst. The other 16 zircons yielded $^{206}Pb/^{238}U$ ages of 139.6–142.6 Ma, with a lower intercept age of 141.8 ± 1.1 Ma (MSWD = 0.21) and a weighted mean $^{206}Pb/^{238}U$ age of 141.5 ± 0.8 Ma (MSWD = 0.22, Fig. 7a, b; Table 1), which may represent the crystallization age.

For the RL2-1 sample of microcline–albite pegmatite, 14 zircon grains were analyzed (Fig. 5b). Nos. 7 and 12 grains yielded $^{206}Pb/^{238}U$ ages of 166.5 ± 1.3 and 149.0 ± 1.1 Ma, respectively, indicating the occurrence of zircon xenocryst. The age obtained from the No. 02 grain largely deviated from the concordia diagram owing to the effect of common Pb on the $^{207}Pb/^{235}U$ age. The other 11 zircon grains yielded consistent $^{206}Pb/^{238}U$ ages of 136.4–138.4 Ma, with a lower intercept age of 137.0 ± 1.0 Ma (MSWD = 0.13) and a weighted mean $^{206}Pb/^{238}U$ age of 137.1 ± 0.8 Ma (MSWD = 0.15, Fig. 7c, d; Table 1), indicating the crystallization age.

For the RL47-1 sample of spodumene–albite pegmatite, 16 zircons were analyzed. Nos. 07, 12, and 16 grains yielded old $^{206}Pb/^{238}U$ ages of 151.4–165.8 Ma, consistent with those of the inherited zircons from the RL7-2 and RL2-1 samples within error. Nos. 04 and 08 grains yielded young $^{206}Pb/^{238}U$ ages of 99.4 and 111.4 Ma, respectively, probably caused by significant Pb loss due to metamictization. The other 11 zircon grains yielded a $^{206}Pb/^{238}U$ age population of 132.7–135.7 Ma, with a lower intercept age of 134.3 ± 1.6 Ma (MSWD = 0.43) and a weighted mean $^{206}Pb/^{238}U$ age of 134.5 ± 0.8 Ma (MSWD = 0.38, Fig. 7e, f; Table 1), representing the crystallization age.

Table 1
Zircon U-Pb dating results of the Renli pegmatite.

| Spot.no.	Content (ppm)		Th/U	Isotopic ratios and 1σ errors							Corrected ages and ± 1σ errors(Ma)					
	^{232}Th	^{238}U		^{207}Pb/^{206}Pb	1σ	^{207}Pb/^{235}U	1σ	^{206}Pb/^{238}U	1σ		^{207}Pb/^{206}Pb	1σ	^{207}Pb/^{235}U	1σ	^{206}Pb/^{238}U	1σ
RL7-2–01	262	13,681	0.02	0.04837	0.00078	0.15049	0.00285	0.02226	0.00034		116.8	37.0	142.3	2.5	141.9	2.1
RL7-2–02	301	13,301	0.02	0.05058	0.00077	0.15711	0.00295	0.02210	0.00026		220.4	35.2	148.2	2.6	140.9	1.7
RL7-2–03	515	17,752	0.03	0.04824	0.00075	0.15012	0.00273	0.02221	0.00029		109.4	37.0	142.0	2.4	141.6	1.8
RL7-2–04	481	16,973	0.03	0.04808	0.00080	0.14968	0.00274	0.02221	0.00027		101.9	38.9	141.6	2.4	141.6	1.7
RL7-2–05	540	20,961	0.03	0.05069	0.00076	0.15738	0.00293	0.02203	0.00026		233.4	35.2	148.4	2.6	140.5	1.6
RL7-2–06	494	19,119	0.03	0.04850	0.00069	0.15208	0.00242	0.02229	0.00023		124.2	33.3	143.7	2.1	142.1	1.4
RL7-2–07	149	5161	0.03	0.04925	0.00081	0.15278	0.00247	0.02211	0.00019		166.8	38.9	144.4	2.2	141.0	1.2
RL7-2–08	301	13,432	0.02	0.05040	0.00081	0.15519	0.00285	0.02189	0.00028		213.0	37.0	146.5	2.5	139.6	1.8
RL7-2–09	394	16,175	0.02	0.05055	0.00080	0.16774	0.00248	0.02355	0.00015		220.4	37.0	157.5	2.2	150.1	1.0
RL7-2–10	392	16,224	0.02	0.05180	0.00085	0.16231	0.00280	0.02225	0.00024		276.0	41.7	152.7	2.4	141.8	1.5
RL7-2–11	240	11,569	0.02	0.04818	0.00082	0.15121	0.00269	0.02224	0.00023		109.4	34.3	143.0	2.4	141.8	1.4
RL7-2–12	369	15,831	0.02	0.04890	0.00077	0.15424	0.00260	0.02237	0.00024		142.7	41.7	145.6	2.3	142.6	1.5
RL7-2–13	620	21,886	0.03	0.05154	0.00080	0.16062	0.00237	0.02217	0.00021		264.9	37.0	151.2	2.1	141.3	1.4
RL7-2–14	312	15,240	0.02	0.04861	0.00073	0.15284	0.00250	0.02230	0.00023		127.9	32.4	144.4	2.2	142.2	1.4
RL7-2–15	502	21,170	0.02	0.04856	0.00073	0.15161	0.00247	0.02215	0.00023		127.9	30.6	143.3	2.2	141.2	1.5
RL7-2–16	442	16,775	0.03	0.04775	0.00070	0.14996	0.00237	0.02230	0.00023		87.1	35.2	141.9	2.1	142.2	1.4
RL7-2–17	369	15,769	0.02	0.04951	0.00077	0.15532	0.00285	0.02228	0.00029		172.3	4.6	146.6	2.5	142.1	1.8
RL7-2–18	82.2	5354	0.02	0.04914	0.00086	0.16172	0.00272	0.02346	0.00023		153.8	36.1	152.2	2.4	149.5	1.4
RL2-1–01	1260	28,673	0.04	0.05500	0.00092	0.16485	0.00280	0.02157	0.00024		413.0	37.0	154.9	2.4	137.6	1.5
RL2-1–02	2725	33,633	0.08	0.09234	0.00217	0.27988	0.00774	0.02160	0.00023		1475.9	44.4	250.6	6.1	137.8	1.4
RL2-1–03	1037	21,431	0.05	0.05782	0.00164	0.17659	0.00637	0.02171	0.00034		524.1	61.1	165.1	5.5	138.4	2.2
RL2-1–04	3749	45,584	0.08	0.05347	0.00104	0.16133	0.00308	0.02146	0.00020		350.1	42.6	151.9	2.7	136.9	1.2
RL2-1–05	1969	27,434	0.07	0.05237	0.00123	0.15892	0.00387	0.02159	0.00030		301.9	49.1	149.8	3.4	137.7	1.9
RL2-1–06	744	16,729	0.04	0.04984	0.00103	0.15199	0.00342	0.02166	0.00036		187.1	48.1	143.7	3.0	138.1	2.3
RL2-1–07	1387	31,138	0.04	0.05088	0.00093	0.18810	0.00326	0.02617	0.00021		235.3	42.6	175.0	2.8	166.5	1.3
RL2-1–08	2150	24,766	0.09	0.04930	0.00074	0.14827	0.00246	0.02143	0.00018		161.2	35.2	140.4	2.2	136.7	1.1
RL2-1–09	1521	28,848	0.05	0.05134	0.00103	0.15250	0.00322	0.02143	0.00024		257.5	46.3	144.1	2.8	136.7	1.5
RL2-1–10	421	17,567	0.02	0.04980	0.00100	0.14930	0.00355	0.02156	0.00027		187.1	46.3	141.3	3.1	137.5	1.7
RL2-1–11	293	4292	0.07	0.05138	0.00115	0.15323	0.00366	0.02138	0.00022		257.5	51.8	144.8	3.2	136.4	1.4
RL2-1–12	456	20,229	0.02	0.05375	0.00102	0.17597	0.00367	0.02338	0.00017		361.2	75.0	164.6	3.2	149.0	1.1
RL2-1–13	799	29,160	0.03	0.04877	0.00081	0.14700	0.00257	0.02147	0.00024		200.1	38.9	139.3	2.3	136.9	1.5
RL2-1–14	1003	22,893	0.04	0.05293	0.00089	0.16040	0.00318	0.02154	0.00027		324.1	38.9	151.1	2.8	137.4	1.7
RL47-1–01	346	7482	0.05	0.05070	0.00097	0.14909	0.00300	0.02116	0.00021		228	72.2	141.1	2.7	135.0	1.4
RL47-1–02	332	4012	0.08	0.06548	0.00175	0.19309	0.00585	0.02120	0.00033		791	62	179.3	5.0	135.3	2.1
RL47-1–03	448	13,133	0.03	0.05061	0.00110	0.14980	0.00406	0.02128	0.00033		233	50.0	141.7	3.6	135.7	2.1
RL47-1–04	1224	33,028	0.04	0.05088	0.00086	0.10979	0.00195	0.01554	0.00015		235	38.9	105.8	1.8	99.4	1.0
RL47-1–05	1487	11,614	0.13	0.05534	0.00102	0.16236	0.00360	0.02105	0.00024		433	40.7	152.8	3.1	134.3	1.5
RL47-1–06	801	12,531	0.06	0.05459	0.00078	0.15895	0.00225	0.02090	0.00013		394	31.5	149.8	2.0	133.4	0.8
RL47-1–07	6425	17,515	0.37	0.05287	0.00081	0.18498	0.00374	0.02518	0.00045		324	39.8	172.3	3.2	160.3	2.8
RL47-1–08	1635	15,312	0.11	0.05734	0.00099	0.13847	0.00266	0.01743	0.00028		506	38.9	131.7	2.4	111.4	1.7
RL47-1–09	30,401	74,933	0.41	0.05350	0.00105	0.15668	0.00424	0.02080	0.00027		350	44.4	147.8	3.7	132.7	1.7
RL47-1–10	1023	19,724	0.05	0.05333	0.00101	0.15812	0.00327	0.02119	0.00025		343	42.6	149.1	2.9	135.2	1.6
RL2-47–11	2868	24,224	0.12	0.04814	0.00073	0.14221	0.00236	0.02116	0.00023		106	32.4	135.0	2.1	135.0	1.5
RL2-47–12	235	6880	0.03	0.05085	0.00101	0.18425	0.00379	0.02605	0.00038		235	46.3	171.7	3.3	165.8	2.4
RL2-47–13	674	19,012	0.04	0.05968	0.00112	0.17783	0.00471	0.02117	0.00031		591	40.7	166.2	4.1	135.1	2.0
RL2-47–14	3366	19,083	0.18	0.06209	0.00176	0.18821	0.00940	0.02113	0.00037		676	63.9	175.1	8.0	134.8	2.4
RL2-47–15	1359	24,812	0.05	0.05697	0.00096	0.16756	0.00259	0.02108	0.00024		500	37.0	157.3	2.3	134.5	1.5
RL2-47–16	553	18,075	0.03	0.05391	0.00111	0.17891	0.00390	0.02377	0.00029		369	46.3	167.1	3.4	151.4	1.8
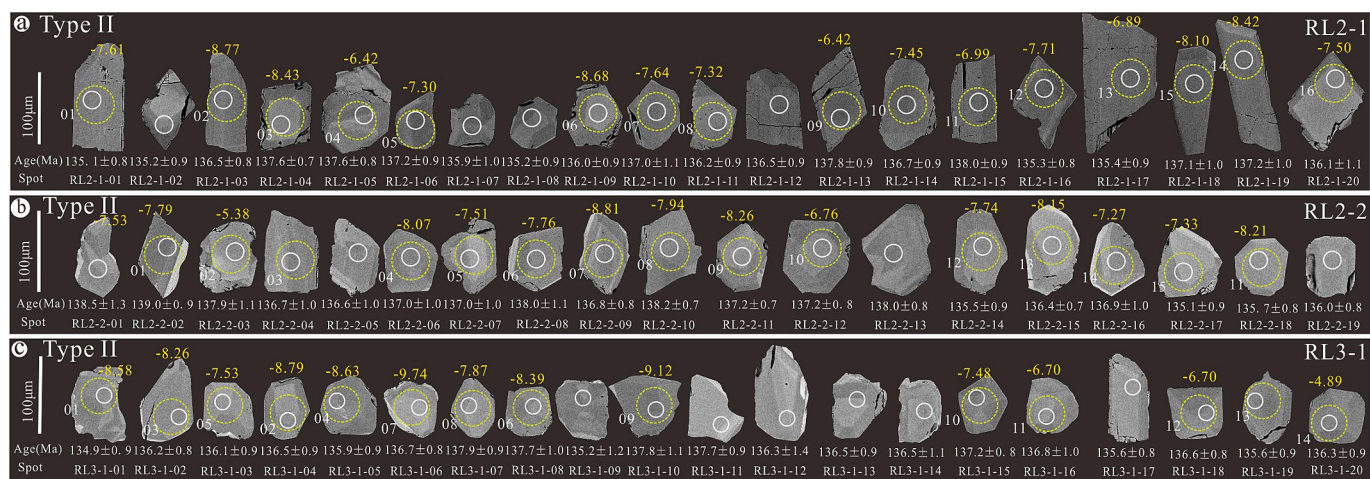
Fig. 6. CL images of monazites the Renli pegmatite. White and yellow circles indicate the laser spots of U–Th–Pb dating and Nd isotope analysis, respectively.

6.4. Monazite U–Th–Pb ages

Although monazite incorporates significant amounts of ^{230}Th into its structure during crystallization, the effect of excess ^{206}Pb from the decay of initial ^{230}Th (Schärer, 1984) can be avoided by using of the Th–Pb system. Monazites typically contain a relatively low amount of radiogenic ^{207}Pb, affording ^{207}Pb/^{235}U ages less precise than ^{206}Pb/^{238}U and ^{208}Pb/^{232}Th ages. The analyzed monazites contain abundant ^{232}Th (Table 2) and significant ^{208}Pb, with high Th/U ratios of 2.6 to 37.2 (average 9.8). Because Th–Pb dating of monazite has advantages over the U–Pb dating because of better counting statistics and smaller proportion of common ^{208}Pb, we adopted the ^{208}Pb/^{232}Th age as the best candidate for the crystallization time of monazite (e.g., Ayers et al., 2002; Cottle et al., 2015; Xiong et al., 2020; Ying et al., 2017).

LA–ICP-MS U–Th–Pb dating was performed on the three groups of monazite samples from microcline–albite pegmatite (RL2-1, RL2-2, and RL3-1) (Fig. 6). Table 2 lists the dating results.

Twenty monazite grains from the RL2-1 sample yielded consistent ^{208}Pb/^{232}Th ages of 135.1–138.0 Ma, with a weighted mean ^{208}Pb/^{232}Th age of 136.5 ± 0.4 Ma (MSWD = 1.12, Fig. 8a, b; Table 2). Nineteen spots on 19 monazite grains from the RL2-2 sample defined a ^{208}Pb/^{232}Th age population of 135.1–139.0 Ma, with a weighted mean ^{208}Pb/^{232}Th age of 137.0 ± 0.5 Ma (MSWD = 1.5, Fig. 8c, d; Table 2). Twenty spots on 20 monazite grains from the RL3-1 sample yielded ^{208}Pb/^{232}Th ages between 134.9 and 137.9 Ma, with a weighted mean ^{208}Pb/^{232}Th age of 136.5 ± 0.4 Ma (MSWD = 0.82, Fig. 8a, b; Table 2).

6.5. Zircon Hf isotope composition

The zircons analyzed for U–Pb age were chosen for Hf isotopic composition analysis. Fig. 5 shows the specific ablation spots, and Table 3 lists the results.

The zircons from RL7-2 have ^{176}Lu/^{177}Hf and ^{176}Hf/^{177}Hf ratios of 0.000673–0.002803 and 0.282443–0.282523, respectively. According to the U–Pb ages, the $\varepsilon_{Hf}(t)$ values are calculated to be − 8.69 to − 5.86 (average − 7.29), the $f_{Lu/Hf}$ values are measured to be − 0.98 to − 0.92, and the T_{DM2} ages are calculated to be 1535 to 1740 Ma (average 1652 Ma).

For RL2-2, the Hf isotope compositions of the zircons from RL2-2 are similar to those of RL7-2: ^{176}Lu/^{177}Hf ratios of 0.000048–0.001929, ^{176}Hf/^{177}Hf ratios of 0.282436–0.282533, $\varepsilon_{Hf}(t)$ values of − 8.87 to − 5.42 (average − 6.58), $f_{Lu/Hf}$ from − 1.00 to − 0.94, and T_{DM2} ages of 1513–1748 Ma (average 1606 Ma).

Zircons from RL47-1 have ^{176}Lu/^{177}Hf and ^{176}Hf/^{177}Hf ratios of 0.000031–0.000122 and 0.282432–0.282570, respectively. The calculated $\varepsilon_{Hf}(t)$ values are − 9.07 to − 4.18 (average − 6.26), the $f_{Lu/Hf}$

values are − 1.00, and the T_{DM2} ages are 1451–1759 Ma (average 1582 Ma).

6.6. Monazite Nd isotope composition

Sm–Nd isotope composition analysis was conducted on euhedral or large monazite grains with concordant U–Th–Pb age from the RL2-1, RL2-2, and RL3-1 samples, with the ablation site overlying the U–Th–Pb spots (Fig. 6). Table 4 lists the results.

For the RL2-1 sample, 16 monazites were analyzed (Fig. 6a). The results are as follows. ^{143}Nd/^{144}Nd ratios of 0.512153–0.512309 with ^{147}Sm/^{144}Nd ratios of 0.13–0.20, $\varepsilon_{Nd}(t)$ of − 8.77 to − 6.42 (average − 7.60), and T_{DM2} ages of 1452–1643 Ma (average 1548 Ma).

For the RL2-2 sample, 15 monazites were analyzed (Fig. 6b). The results are as follows. ^{143}Nd/^{144}Nd ratios of 0.512144–0.512322 with ^{147}Sm/^{144}Nd ratios of 0.13–0.17. The corresponding $\varepsilon_{Nd}(t)$ values are between − 8.81 and − 5.38 (average − 7.62), and T_{DM2} ages are 1368–1647 Ma (average 1549 Ma).

For the RL3-1 sample, the results for the Nd isotope compositions of the monazite grains are as follows: ^{147}Sm/^{144}Nd ratios of 0.512093–0.512387 with ^{147}Sm/^{144}Nd ratios of 0.14–0.20, $\varepsilon_{Nd}(t)$ values of − 9.74 to − 4.89 (average − 7.94), and T_{DM2} ages of 1328 to 1721 Ma (average 1575 Ma).

7. Discussion

7.1. Geochronology of the Renli pegmatite

Granitic pegmatites commonly contain certain amounts of accessory and ore minerals, such as zircon, apatite, monazite, and columbite group minerals, which are adaptable for dating. Zircon and monazite were chosen because of the high closure temperature of the U–Pb system (>600 °C; Mezger et al., 1989; Sevigny and Hanson, 1992) and the wide application of zircon Hf and monazite Nd isotope compositions. The zircon grains collected from RL7-2, RL2-1, and RL47-1 display weak luminescence (Fig. 3), high U and Th contents, and low Th/U ratios (Table 1), which are distinct from the typical magmatic zircon described by Hoskin and Schaltegger (2003). However, it is difficult to exclude the magmatic origin of these zircons by the features mentioned above. For instance, the weak luminescence of zircon probably results from the suppression of CL emission caused by high U^{4+} abundance and its radiation damage on the crystal lattice (Nasdala et al., 2003). In addition, the very low Th/U ratio can be ascribed to the preferential incorporation of U^{4+} into zircon owing to its small ionic radius compared to Th^{4+} and the large partition coefficient of U compared to Th in H$_2$O-rich fluids (Rollinson and Windley, 1980). In addition, some zircons from the RL7-

Table 2
Monazite U-Th-Pb dating results of theRenli pegmatite.

| Spot.no.	Content (ppm)			Common Pb	Isotopic ratios and 1σ errors						Corrected ages and ± 1σ errors(Ma)							
	Pb(Total)	232Th	238U		207Pb/235U	1σ	206Pb/238U	1σ	208Pb/232Th	1σ	207Pb/206Pb	1σ	207Pb/235U	1σ	206Pb/238U	1σ	208Pb/232Th	1σ
RL2-1–01	1582	195,894	24,197	0.5	0.15150	0.00290	0.02124	0.00017	0.00671	0.00004	333.4	40.7	143.2	2.6	135.5	1.0	135.1	0.8
RL2-1–02	1327	146,232	25,447	5.8	0.15004	0.00262	0.02120	0.00016	0.00671	0.00004	253.8	38.9	141.9	2.3	135.2	1.0	135.2	0.9
RL2-1–03	1554	179,255	27,157	6.8	0.14876	0.00250	0.02131	0.00015	0.00678	0.00004	220.4	37.0	140.8	2.2	135.9	1.0	136.5	0.8
RL2-1–04	2030	232,388	35,883	4.6	0.14753	0.00212	0.02130	0.00013	0.00683	0.00004	211.2	31.5	139.7	1.9	135.9	0.8	137.6	0.7
RL2-1–05	1667	175,314	34,534	5.6	0.14587	0.00237	0.02103	0.00017	0.00683	0.00004	205.6	35.2	138.3	2.1	134.2	1.1	137.6	0.8
RL2-1–06	1469	172,576	25,033	3.3	0.14798	0.00242	0.02138	0.00015	0.00681	0.00004	198.2	33.3	140.1	2.1	136.4	0.9	137.2	0.9
RL2-1–07	1050	115,539	21,221	2.8	0.15051	0.00288	0.02082	0.00020	0.00675	0.00005	298.2	41.7	142.4	2.5	132.9	1.3	135.9	1.0
RL2-1–08	1390	172,499	22,215	3.8	0.14945	0.00265	0.02115	0.00016	0.00671	0.00004	255.6	37.0	141.4	2.3	134.9	1.0	135.2	0.9
RL2-1–09	1784	199,284	34,676	3.0	0.14961	0.00233	0.02114	0.00017	0.00675	0.00004	253.8	31.5	141.6	2.1	134.8	1.1	136.0	0.9
RL2-1–10	1439	178,569	22,456	9.6	0.14919	0.00292	0.02155	0.00021	0.00680	0.00005	211.2	44.4	141.2	2.6	137.5	1.3	137.0	1.1
RL2-1–11	1589	207,782	22,035	9.0	0.14826	0.00263	0.02141	0.00019	0.00676	0.00005	205.6	37.0	140.4	2.3	136.6	1.2	136.2	0.9
RL2-1–12	1444	171,205	24,788	0.8	0.14860	0.00252	0.02130	0.00015	0.00678	0.00004	220.4	37.0	140.7	2.2	135.9	1.0	136.5	0.9
RL2-1–13	1569	171,543	30,348	0.4	0.14971	0.00228	0.02141	0.00017	0.00684	0.00005	233.4	31.5	141.7	2.0	136.5	1.1	137.8	0.9
RL2-1–14	1546	185,470	25,637	2.3	0.15034	0.00285	0.02135	0.00016	0.00679	0.00004	239.0	40.7	142.2	2.5	136.2	1.0	136.7	0.9
RL2-1–15	1230	150,858	19,069	4.4	0.15261	0.00277	0.02135	0.00017	0.00685	0.00005	279.7	40.7	144.2	2.4	136.2	1.1	138.0	0.9
RL2-1–16	1523	155,648	33,273	1.7	0.14854	0.00238	0.02123	0.00018	0.00672	0.00004	233.4	31.5	140.6	2.1	135.4	1.1	135.3	0.8
RL2-1–17	1259	164,672	17,338	6.4	0.15234	0.00303	0.02129	0.00016	0.00672	0.00005	276.0	42.6	144.0	2.7	135.8	1.0	135.4	0.9
RL2-1–18	1656	191,548	29,525	4.1	0.14331	0.00250	0.02111	0.00016	0.00681	0.00005	153.8	37.0	136.0	2.2	134.7	1.0	137.1	1.0
RL2-1–19	1920	240,717	28,038	3.2	0.14766	0.00249	0.02143	0.00017	0.00681	0.00005	190.8	39.8	139.8	2.2	136.7	1.1	137.2	1.0
RL2-1–20	1744	208,827	28,865	7.3	0.14968	0.00257	0.02123	0.00016	0.00676	0.00005	242.7	37.0	141.6	2.3	135.4	1.0	136.1	1.1
RL2-2–01	1428	148,079	30,104	10.9	0.15842	0.00299	0.02161	0.00018	0.00688	0.00006	344.5	36.1	149.3	2.6	137.8	1.2	138.5	1.3
RL2-2–02	1710	182,486	34,749	9.0	0.15253	0.00237	0.02138	0.00018	0.00690	0.00005	333.4	31.5	144.1	2.1	136.3	1.1	139.0	0.9
RL2-2–03	1685	211,484	25,320	4.7	0.15321	0.00264	0.02169	0.00019	0.00684	0.00005	253.8	43.5	144.7	2.3	138.3	1.2	137.9	1.1
RL2-2–04	1683	180,693	34,789	7.5	0.14592	0.00239	0.02131	0.00016	0.00678	0.00005	176.0	37.0	138.3	2.1	135.9	1.0	136.7	1.0
RL2-2–05	1504	179,008	25,851	3.6	0.15034	0.00257	0.02145	0.00018	0.00678	0.00005	231.6	69.4	142.2	2.3	136.8	1.1	136.6	1.0
RL2-2–06	1547	152,283	35,912	5.8	0.14628	0.00240	0.02115	0.00017	0.00680	0.00005	211.2	35.2	138.6	2.1	134.9	1.1	137.0	1.0
RL2-2–07	1899	244,897	26,679	7.5	0.15062	0.00281	0.02171	0.00019	0.00680	0.00005	211.2	37.0	142.5	2.5	138.5	1.2	137.0	1.0
RL2-2–08	1380	173,150	20,850	9.9	0.15149	0.00288	0.02133	0.00024	0.00685	0.00006	264.9	36.1	143.2	2.5	136.0	1.5	138.0	1.1
RL2-2–09	1898	222,870	32,919	4.2	0.14783	0.00240	0.02151	0.00016	0.00679	0.00004	187.1	35.2	140.0	2.1	137.2	1.0	136.8	0.8
RL2-2–10	1240	175,933	12,313	7.4	0.14928	0.00356	0.02190	0.00015	0.00686	0.00004	164.9	53.7	141.3	3.1	139.6	1.0	138.2	0.7
RL2-2–11	1900	215,446	34,884	5.7	0.14644	0.00207	0.02145	0.00013	0.00681	0.00004	168.6	−0.9	138.8	1.8	136.8	0.8	137.2	0.7
RL2-2–12	1638	222,032	19,589	5.0	0.14961	0.00272	0.02152	0.00018	0.00681	0.00004	213.0	40.7	141.6	2.4	137.3	1.2	137.2	0.8
RL2-2–13	1216	138,250	21,826	5.8	0.14630	0.00236	0.02137	0.00014	0.00685	0.00004	176.0	35.2	138.6	2.1	136.3	0.9	138.0	0.8
RL2-2–14	1806	219,452	28,946	7.4	0.13863	0.00235	0.02116	0.00017	0.00672	0.00005	76.0	35.2	131.8	2.1	135.0	1.1	135.5	0.9
RL2-2–15	1510	177,188	25,681	6.3	0.13872	0.00250	0.02095	0.00014	0.00677	0.00004	101.9	38.9	131.9	2.2	133.6	0.9	136.4	0.7
RL2-2–16	1267	160,468	18,109	3.9	0.14090	0.00288	0.02096	0.00019	0.00679	0.00005	139.0	45.4	133.8	2.6	133.7	1.2	136.9	1.0
RL2-2–17	1661	202,878	26,530	8.3	0.13225	0.00241	0.02070	0.00016	0.00670	0.00004	20.5	40.7	126.1	2.2	132.1	1.0	135.1	0.9
RL2-2–18	1612	188,794	27,938	5.0	0.13175	0.00233	0.02046	0.00016	0.00674	0.00004	53.8	43.5	125.7	2.1	130.5	1.0	135.7	0.8
RL2-2–19	1448	175,624	23,354	6.2	0.13043	0.00245	0.02035	0.00017	0.00675	0.00004	39.0	−162.0	124.5	2.2	129.9	1.1	136.0	0.8
RL3-1–01	1258	118,772	30,843	4.0	0.14805	0.00253	0.02103	0.00016	0.00670	0.00004	239.0	32.4	140.2	2.2	134.1	1.0	134.9	0.9
RL3-1–02	1670	156,337	41,618	6.0	0.14451	0.00213	0.02088	0.00015	0.00676	0.00004	211.2	31.5	137.1	1.9	133.2	0.9	136.2	0.8
RL3-1–03	1382	135,250	32,966	6.5	0.14842	0.00232	0.02103	0.00016	0.00676	0.00005	255.6	33.3	140.5	2.1	134.2	1.0	136.1	0.9
RL3-1–04	1720	143,535	48,759	9.0	0.14519	0.00213	0.02087	0.00015	0.00678	0.00004	209.3	25.0	137.7	1.9	133.2	1.0	136.5	0.9
RL3-1–05	1561	132,416	43,555	6.8	0.14913	0.00228	0.02104	0.00017	0.00675	0.00005	257.5	26.9	141.1	2.0	134.2	1.1	135.9	0.9
RL3-1–06	1810	185,408	41,443	11.5	0.14803	0.00210	0.02103	0.00015	0.00679	0.00004	239.0	62.0	140.2	1.9	134.2	1.0	136.7	0.8
RL3-1–07	1918	180,318	48,187	6.7	0.14734	0.00236	0.02107	0.00017	0.00685	0.00005	233.4	33.3	139.6	2.1	134.4	1.0	137.9	0.9
RL3-1–08	1781	166,380	45,575	7.4	0.14780	0.00237	0.02077	0.00017	0.00684	0.00005	264.9	33.3	140.0	2.1	132.5	1.1	137.7	1.0
RL3-1–09	1699	143,574	48,894	15.3	0.14822	0.00269	0.02068	0.00022	0.00671	0.00006	283.4	34.3	140.3	2.4	132.0	1.4	135.2	1.2
RL3-1–10	1335	118,737	35,201	6.4	0.14894	0.00260	0.02116	0.00018	0.00684	0.00005	239.0	32.4	141.0	2.3	135.0	0.9	137.8	1.1
RL3-1–11	3054	265,815	82,616	10.0	0.15005	0.00206	0.02103	0.00017	0.00684	0.00004	333.4	25.9	142.0	1.8	134.2	1.0	137.7	0.9
RL3-1–12	2401	199,801	67,957	5.9	0.15032	0.00262	0.02088	0.00023	0.00677	0.00007	300.1	35.2	142.2	2.3	133.2	1.4	136.3	1.4
RL3-1–13	2496	209,077	70,659	7.8	0.14621	0.00211	0.02068	0.00017	0.00678	0.00004	250.1	29.6	138.6	1.9	132.0	1.1	136.5	0.9
RL3-1–14	2585	202,549	77,270	12.4	0.14710	0.00246	0.02069	0.00021	0.00678	0.00005	261.2	31.5	139.4	2.2	132.0	1.3	136.5	1.1
RL3-1–15	1723	158,454	43,236	10.1	0.15145	0.00264	0.02114	0.00015	0.00681	0.00005	276.0	39.8	143.2	2.3	134.9	0.9	137.2	0.8
RL3-1–16	1865	180,899	44,475	4.8	0.14795	0.00240	0.02104	0.00017	0.00679	0.00005	239.0	30.6	140.1	2.1	134.2	1.1	136.8	1.0
RL3-1–17	2824	254,639	75,144	6.2	0.14576	0.00194	0.02051	0.00013	0.00673	0.00004	261.2	24.1	138.2	1.7	130.9	0.8	135.6	0.8
RL3-1–18	1726	165,226	41,774	6.5	0.14771	0.00243	0.02089	0.00014	0.00678	0.00004	250.1	35.2	139.9	2.2	133.3	0.9	136.6	0.8
RL3-1–19	1787	166,262	45,280	7.8	0.14290	0.00209	0.02078	0.00016	0.00673	0.00004	187.1	25.0	135.6	1.9	132.6	1.0	135.6	0.9
RL3-1–20	1998	192,709	48,407	2.8	0.14678	0.00237	0.02070	0.00016	0.00676	0.00004	253.8	31.5	139.1	2.1	132.1	1.0	136.3	0.9
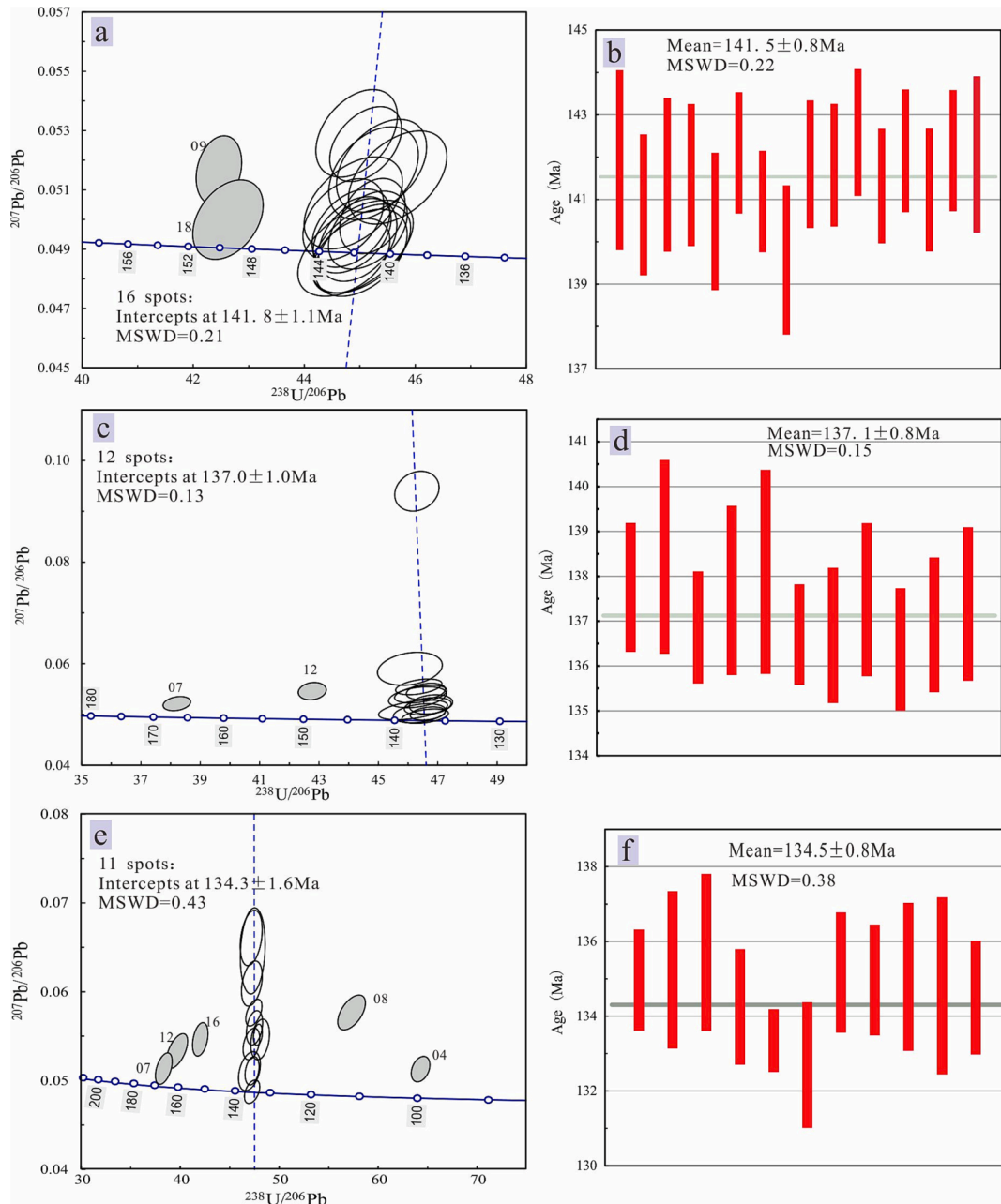
Fig. 7. Tera-Wasserburg of zircon U–Pb age plots (a, c, and e) and weighted average age diagrams (b, d, and f) of the Renli Nos. 7, 2 and 47 pegmatites, respectively.

2, RL2-1, and RL47-1 samples feature growth zoning in CL images, which supports a magmatic origin.

However, most zircons from the Nos. 2, 7 and 47 pegmatites are highly rich in U (4012–33028 ppm), with low Th/U ratios (mostly below 0.1) (Table 1), and weak or mosaic luminescence (Fig. 5), indicating that they suffered from later reworking event(s). A high abundance of U and its radioactive decay destroys the zircon lattice, i.e., metamictization, and make zircons susceptive to fluid alteration, leaching, and recrystallization, which is featured by spongy texture and mosaic luminescence. The loss of radiogenic Pb daughters lose from metamict zircons occurs through diffusion because their large ionic radius will induce younger U-Pb ages. In addition, the $^{206}Pb/^{238}U$ and $^{207}Pb/^{235}U$ ages obtained from metamict zircons reworked by later fluids could be discordant in most cases, with discordant younger ages owing to Pb-losing induced by fluid leaching or older ages owing to the incorporation of common Pb in zircon. The recrystallization effect on U-Pb age depends on the degree and time of recrystallization: the former affects

the age concordance and the latter determines whether it can be distinguished from zircon crystallization age under specific conditions of analysis technique. However, mostly concordant $^{206}Pb/^{238}U$ and $^{207}Pb/^{235}U$ ages are obtained from the zircons (with concordance > 90 %), indicating limited effect from Pb losing and acquisition. In addition, zircons from the early pegmatites, such as the No. 7 pegmatite (type I) and the No. 2 pegmatite (type II), have distinct $^{206}Pb/^{238}U$ ages from those of the late pegmatites, such as the No. 47 pegmatite (type III), indicating the limited effect from multistage magmatic activities. Zircons from RL2-1 pegmatite show a weighted average $^{206}Pb/^{238}U$ age of 137.1 ± 0.8 Ma, which is consistent with that obtained from the monazite of the same sample (137.0 ± 0.5 Ma). These ages are evidently older than the upper age limit of the same type of pegmatite represented by the Ar–Ar (125.0 ± 1.40 Ma) and Re–Os ages (130.1 ± 1.1 Ma), such as the No.5 pegmatite, Considering the high closure temperatures of U-Pb system in zircon and monazite (>600 °C, Cherniak and Watson, 2000; Compeland, 1990) as compared to those of muscovite Ar-Ar
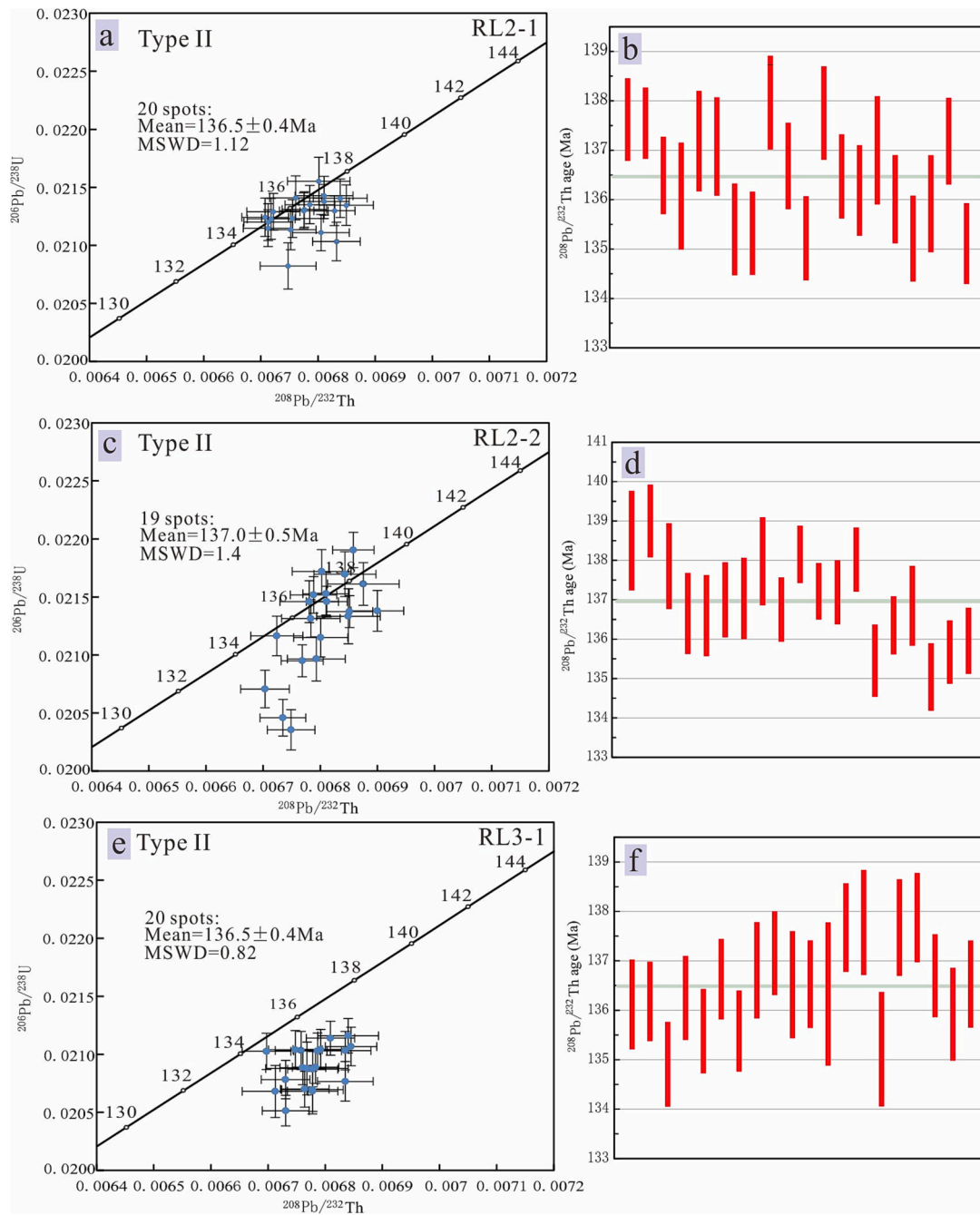
Fig. 8. Monazite U–Th–Pbconcordia age plots (a, c, and e) and weighted average diagrams (b, d, and f) of the Renli No. 2, later intrusion dike, and No. 3 pegmatites, respectively.

(425 °C, Harrison et al., 2009) and molybdenite re-Os (500 °C, Suzuki et al., 1996), there is no doubt that the zircon U-Pb ages were free from late thermal events.

In some cases, metamictization could magnify the apparent age because of a "high U effect" (Williams and Hergt, 2000; Li et al., 2013). In Fig. 9, the apparent $^{206}Pb/^{238}U$ ages do not show a positive or negative correlation with the U contents of zircon (Fig. 9a); similarly, the apparent $^{208}Pb/^{232}Th$ ages are independent of the U and Th contents of monazite (Fig. 9b and c), implying limited effects of high U and Th contents on the apparent $^{206}Pb/^{238}U$ and $^{208}Pb/^{232}Th$ ages, respectively. It has been demonstrated that a high U effect is mainly observed in the dating results by secondary-ion mass spectrometry rather than LA–ICP–MS (Zhao et al., 2014; Zhang et al., 2017), and the $^{208}Pb/^{232}Th$ ages obtained from Th-rich monazite are also consistent with the zircon

or coltan U–Pb age proven by another group (Xiong et al., 2020) and this study (see ages of RL2-2 in Fig. 7c and 8c). Therefore, our zircon and monazite U–Pb ages can represent the formation times of the studied pegmatites.

To ensure the accuracy of the U–Pb ages for the different types of pegmatite in the Renli mining area, both zircon U–Pb and monazite U–Th–Pb geochronology studies were performed on the Renli pegmatites. The RL2-2 from the No. 2 pegmatite (type II) gave a zircon U–Pb age of 137.1 ± 0.8 Ma (Fig. 7c, d), Which is consistent with the monazite Th–Pb age of 137.0 ± 0.5 Ma (Fig. 8c, d) within the range of error, indicating that both zircon U–Pb and monazite Th–Pb ages are mutually supportive and convincible. The RL7-2 sample from the No. 7 pegmatite (type I) gave a zircon $^{206}Pb/^{238}U$ age of 141.5 ± 0.8 Ma (Fig. 7a, b), while the RL47-1 sample from the No. 47 pegmatite (type III) gave a

Table 3
Zircon Hf isotopic compositions of the Renli pegmatites.

Spot no.	Age (Ma)	$^{176}Yb/^{177}Hf$	$^{176}Lu/^{177}Hf$	$^{176}Hf/^{177}Hf$	2σ	εHf(0)	εHf(t)	T_{DM1}	T_{DM2}	$f_{Lu/Hf}$
RL7-2–01	141.9	0.039240	0.001114	0.282475	0.000011	−10.52	−7.51	1102	1666	−0.97
RL7-2–02	140.9	0.020978	0.000629	0.282493	0.000008	−9.86	−6.83	1063	1622	−0.98
RL7-2–03	141.6	0.021658	0.000721	0.282503	0.000013	−9.52	−6.49	1052	1601	−0.98
RL7-2–04	141.6	0.034302	0.001013	0.282490	0.000009	−9.96	−6.95	1077	1630	−0.97
RL7-2–05	142.8	0.045529	0.001350	0.282490	0.000008	−9.98	−6.97	1088	1633	−0.96
RL7-2–06	142.1	0.040751	0.001235	0.282500	0.000009	−9.61	−6.61	1070	1609	−0.96
RL7-2–07	141.0	0.025670	0.000673	0.282477	0.000011	−10.45	−7.42	1087	1659	−0.98
RL7-2–08	139.6	0.029114	0.000793	0.282451	0.000009	−11.37	−8.38	1127	1719	−0.98
RL7-2–09	150.1	0.014481	0.000487	0.282513	0.000007	−9.16	−5.92	1031	1572	−0.99
RL7-2–10	141.8	0.049005	0.001607	0.282523	0.000009	−8.82	−5.86	1048	1561	−0.95
RL7-2–11	141.8	0.066265	0.002248	0.282503	0.000008	−9.51	−6.61	1095	1609	−0.93
RL7-2–12	142.6	0.040757	0.001247	0.282495	0.000009	−9.81	−6.80	1078	1622	−0.96
RL7-2–13	141.3	0.082928	0.002748	0.282452	0.000009	−11.32	−8.48	1186	1726	−0.92
RL7-2–14	142.2	0.054018	0.001652	0.282443	0.000008	−11.65	−8.69	1164	1740	−0.95
RL7-2–15	141.2	0.052622	0.001616	0.282462	0.000008	−10.95	−8.00	1135	1696	−0.95
RL7-2–16	142.2	0.029245	0.000832	0.282490	0.000009	−9.97	−6.93	1072	1629	−0.97
RL7-2–17	142.1	0.072106	0.002803	0.282461	0.000010	−11.01	−8.15	1175	1706	−0.92
RL7-2–18	149.5	0.023870	0.000613	0.282530	0.000010	−8.56	−5.34	1011	1535	−0.98
RL2-1–01	137.6	0.002218	0.000048	0.282436	0.000007	−11.88	−8.87	1125	1748	−1.00
RL2-1–02	137.8	0.008493	0.000259	0.282461	0.000010	−11.01	−8.01	1097	1695	−0.99
RL2-1–03	138.4	0.005733	0.000143	0.282477	0.000009	−10.42	−7.40	1071	1656	−1.00
RL2-1–04	136.9	0.005691	0.000133	0.282534	0.000012	−8.41	−5.42	993	1530	−1.00
RL2-1–05	137.7	0.015539	0.000405	0.282513	0.000013	−9.15	−6.16	1028	1578	−0.99
RL2-1–06	138.1	0.023182	0.000523	0.282533	0.000009	−8.45	−5.47	1004	1534	−0.98
RL2-1–07	166.5	0.026489	0.000607	0.282534	0.000008	−8.43	−4.85	1006	1516	−0.98
RL2-1–08	136.7	0.055431	0.001686	0.282442	0.000010	−11.67	−8.83	1166	1745	−0.95
RL2-1–09	136.7	0.009392	0.000238	0.282519	0.000009	−8.95	−5.98	1017	1565	−0.99
RL2-1–10	137.5	0.019882	0.000372	0.282524	0.000011	−8.77	−5.79	1013	1554	−0.99
RL2-1–11	136.4	0.057849	0.001929	0.282482	0.000010	−10.25	−7.43	1116	1657	−0.94
RL2-1–12	149.0	0.008457	0.000143	0.282539	0.000009	−8.25	−5.00	987	1513	−1.00
RL2-1–13	136.9	0.050026	0.001795	0.282495	0.000010	−9.80	−6.96	1094	1627	−0.95
RL2-1–14	137.4	0.056076	0.001722	0.282522	0.000010	−8.85	−5.99	1053	1566	−0.95
RL47-1–01	135.0	0.004557	0.000122	0.282487	0.000008	−10.08	−7.13	1057	1637	−1.00
RL47-1–02	135.3	0.002929	0.000074	0.282502	0.000009	−9.57	−6.61	1036	1604	−1.00
RL47-1–03	135.7	0.002723	0.000069	0.282508	0.000010	−9.33	−6.36	1027	1589	−1.00
RL47-1–04	99.4	0.002653	0.000067	0.282511	0.000010	−9.23	−7.05	1023	1605	−1.00
RL47-1–05	134.3	0.002000	0.000058	0.282432	0.000010	−12.01	−9.07	1130	1759	−1.00
RL47-1–06	133.4	0.002177	0.000054	0.282446	0.000009	−11.51	−8.59	1111	1728	−1.00
RL47-1–07	160.3	0.003288	0.000076	0.282537	0.000010	−8.33	−4.82	988	1510	−1.00
RL47-1–08	111.4	0.005039	0.000110	0.282536	0.000012	−8.34	−5.91	989	1542	−1.00
RL47-1–09	132.7	0.002462	0.000063	0.282501	0.000009	−9.58	−6.67	1036	1606	−1.00
RL47-1–10	135.2	0.002296	0.000061	0.282549	0.000010	−7.88	−4.92	970	1498	−1.00
RL47-1–11	135.0	0.003875	0.000105	0.282570	0.000014	−7.14	−4.18	942	1451	−1.00
RL47-1–12	165.8	0.005089	0.000129	0.282573	0.000014	−7.03	−3.41	939	1425	−1.00
RL47-1–13	135.1	0.002555	0.000075	0.282511	0.000009	−9.22	−6.26	1022	1582	−1.00
RL47-1–14	134.8	0.002742	0.000080	0.282530	0.000009	−8.57	−5.62	997	1541	−1.00
RL47-1–15	134.5	0.001104	0.000031	0.282485	0.000010	−10.15	−7.20	1057	1641	−1.00
RL47-1–16	151.4	0.001460	0.000034	0.282498	0.000010	−9.71	−6.39	1040	1603	−1.00

$\varepsilon_{Hf}(t) = 10,000 \times (\{[(^{176}Hf/^{177}Hf)_S - (^{176}Lu/^{177}Hf)_S \times (e^{\lambda t} - 1)] / [(^{176}Hf/^{177}Hf)_{CHUR, 0} - (^{176}Lu/^{177}Hf)_{CHUR} \times ((e^{\lambda t} - 1)] - 1\})$. $T_{DM} = 1/\lambda \times \ln\{1 + [(^{176}Hf/^{177}Hf)_S - (^{176}Hf/^{177}Hf)_{DM}] / [(^{176}Hf/^{177}Hf)_S - (^{176}Hf/^{177}Hf)_{DM}]\}$. $T_{DM C} = T_{DM} - (T_{DM} - t) \times [(f_{cc} - f_s) / (f_{cc} - f_{DM})]$. $f Lu/Hf = (^{176}Lu/^{177}Hf)_S / (^{176}Lu/^{177}Hf)_{CHUR} - 1$, where, $\lambda = 1.867 \times 10^{-11}$/a (Soderlund et al., 2004); $(^{176}Lu/^{177}Hf)_S$ and $(^{176}Hf/^{177}Hf)_S$ are the measured values of the samples; $(^{176}Lu/^{177}Hf)_{CHUR} = 0.0332$ and $(^{176}Hf/^{177}Hf)_{CHUR,0} = 0.282772$ (Blichert-Toft and Albarède, 1997); $(^{176}Lu/^{177}Hf)_{DM} = 0.0384$ and $(^{176}Hf/^{177}Hf)_{DM} = 0.28325$ (Griffin et al., 2000); $(^{176}Lu/^{177}Hf)_{mean crust} = 0.015$; $f_{cc} = [(^{176}Lu/^{177}Hf)_{mean crust} / (^{176}Lu/^{177}Hf)_{CHUR}] - 1$; $fs = f Lu/Hf$; $f_{DM} = [(^{176}Lu/^{177}Hf)_{DM} / (^{176}Lu/^{177}Hf)_{CHUR}] - 1$; t = crystallization time of zircon.

zircon $^{206}Pb/^{238}U$ age of 134.5 ± 0.8 Ma (Fig. 7e, f). In addition, the RL3-1 from the No. 3 pegmatite (type II) gave a monazite weighted mean $^{208}Pb/^{232}Th$ age of 136.5 ± 0.4 Ma (Fig. 8e, f), and the RL2-1 sample from the late pegmatite intrusion in the No. 2 pegmatite yielded a monazite $^{208}Pb/^{232}Th$ age of 136.5 ± 0.4 Ma (Fig. 8a, b), consistent with the zircon and monazite U–Th–Pb ages of the No. 2 pegmatite within error, indicating the two stages of magma activities in the No.2 pegmatite at least in a very short period of time. In summary, our dating results suggest that (1) the pegmatites were gradually formed from type I to type III with distance from the YMB and with time from ca. 141 to 134 Ma; and (2) the formation ages are virtually unanimous for the same type of pegmatite but evidently distinguishable for different types of pegmatite.

7.2. Genetic relationship between pegmatite and granite

It has been suggested that rare-metal pegmatites can be formed by the anatexis of sedimentary rocks without parental granites (Barros and Menuge, 2016; Dill, 2015, 2016; Knoll et al., 2018; Lv et al., 2018, 2021b; Müller et al., 2017; Zhang et al., 2019); meanwhile, it is commonly believed that pegmatites originate from the crystallization differentiation of granitic magmas (Černy and Ercit, 2005; Černy et al., 2012; London, 2014, 2018, London et al., 2020; Roda-Robles et al., 2018). The pegmatite regional zoning around the Mufushan batholith in the Renli area (Fig. 2) suggests a closely spatial relationship between the Mufushan granites and Renli pegmatites. In addition, previous chronology studies and the dating results herein suggest a successive activity timeline for the igneous rocks in the YMB (Table 5; Fig. 10). The diorite, granodiorite, BMG, two-mica granite, and MMG have zircon U–Pb ages of 154.0 ± 1.9, 151.5 ± 1.3, 154–140, 146–138, and 141.0 ± 1.2 Ma,

Table 4
Monazite Nd isotopic data of the Renli pegmatite.

spot	Age(Ma)	$^{147}Sm/^{144}Nd$	$^{143}Nd/^{144}Nd$	2σ	εNd(0)	εNd(t)	T_{DM}	T_{DM2}
RL2-1–01	136.5	0.1525427	0.5122086	0.000028	−8.38	−7.61	2342	1549
RL2-1–02	136.5	0.1569837	0.5121531	0.00003	−9.46	−8.77	2672	1643
RL2-1–03	136.5	0.1500268	0.5121642	0.000024	−9.24	−8.43	2355	1615
RL2-1–04	136.5	0.1961955	0.5123087	0.000024	−6.42	−6.42	7226	1452
RL2-1–05	136.5	0.1671111	0.5122375	0.000023	−7.81	−7.30	2975	1524
RL2-1–06	136.5	0.1652963	0.5121652	0.000023	−9.22	−8.68	3089	1635
RL2-1–07	136.5	0.1550979	0.5122091	0.000023	−8.37	−7.64	2442	1552
RL2-1–08	136.5	0.1622110	0.5122321	0.000026	−7.92	−7.32	2710	1525
RL2-1–09	136.5	0.1450644	0.5122629	0.000029	−7.32	−6.42	1969	1452
RL2-1–10	136.5	0.1501454	0.5122145	0.000024	−8.26	−7.45	2240	1536
RL2-1–11	136.5	0.1480716	0.5122366	0.000024	−7.83	−6.99	2119	1498
RL2-1–12	136.5	0.1464113	0.5121981	0.000021	−8.58	−7.71	2153	1557
RL2-1–13	136.5	0.1520852	0.5122452	0.000021	−7.66	−6.89	2235	1490
RL2-1–14	136.5	0.1368375	0.5121532	0.000022	−9.46	−8.42	1975	1614
RL2-1–15	136.5	0.1661190	0.5121958	0.000022	−8.63	−8.10	3046	1588
RL2-1–16	136.5	0.1389485	0.5122022	0.000024	−8.50	−7.50	1931	1540
RL2-2–01	137.0	0.1611028	0.5122201	0.000024	−8.15	−7.53	2688	1543
RL2-2–02	137.0	0.1565784	0.5122030	0.000021	−8.49	−7.79	2521	1564
RL2-2–03	137.0	0.1521509	0.5123223	0.00004	−6.16	−5.38	2048	1368
RL2-2–04	137.0	0.1508650	0.5121834	0.000043	−8.87	−8.07	2340	1586
RL2-2–05	137.0	0.1557368	0.5122163	0.00004	−8.23	−7.51	2450	1541
RL2-2–06	137.0	0.1469657	0.5121958	0.000026	−8.63	−7.76	2176	1561
RL2-2–07	137.0	0.1489083	0.5121437	0.000021	−9.64	−8.81	2363	1647
RL2-2–08	137.0	0.1461180	0.5121856	0.000024	−8.82	−7.94	2172	1576
RL2-2–09	137.0	0.1390080	0.5121632	0.000023	−9.26	−8.26	2012	1602
RL2-2–10	137.0	0.1501978	0.5122501	0.000023	−7.57	−6.76	2157	1480
RL2-2–11	137.0	0.1470500	0.5121727	0.00003	−9.08	−8.21	2231	1598
RL2-2–12	137.0	0.1498649	0.5122133	0.000021	−8.28	−7.47	2233	1538
RL2-2–13	137.0	0.1533907	0.5121815	0.000026	−8.90	−8.15	2442	1593
RL2-2–14	137.0	0.1520429	0.5122256	0.000025	−8.04	−7.27	2282	1521
RL2-2–15	137.0	0.1530462	0.5122232	0.000024	−8.09	−7.33	2325	1527
RL3-1–01	136.5	0.1437782	0.5121508	0.000023	−9.50	−8.58	2175	1628
RL3-1–02	136.5	0.1628774	0.5121573	0.000023	−9.38	−8.79	2967	1645
RL3-1–03	136.5	0.1489253	0.5121720	0.000023	−9.09	−8.26	2297	1602
RL3-1–04	136.5	0.1606525	0.5121633	0.000031	−9.26	−8.63	2826	1632
RL3-1–05	136.5	0.1570257	0.5122168	0.000024	−8.22	−7.53	2504	1542
RL3-1–06	136.5	0.1943988	0.5122060	0.000039	−8.43	−8.39	7346	1612
RL3-1–07	136.5	0.1452257	0.5120930	0.000025	−10.63	−9.74	2348	1721
RL3-1–08	136.5	0.1515641	0.5121946	0.000022	−8.65	−7.87	2339	1570
RL3-1–09	136.5	0.1648371	0.5121420	0.000026	−9.68	−9.12	3132	1672
RL3-1–10	136.5	0.1606383	0.5122224	0.000024	−8.11	−7.48	2658	1538
RL3-1–11	136.5	0.1638258	0.5122651	0.000026	−7.27	−6.70	2698	1475
RL3-1–12	136.5	0.1500175	0.5121992	0.000031	−8.56	−7.75	2272	1560
RL3-1–13	136.5	0.1671529	0.5122302	0.000028	−7.95	−7.44	3002	1535
RL3-1–14	136.5	0.1966343	0.5123871	0.000031	−4.89	−4.89	6734	1328
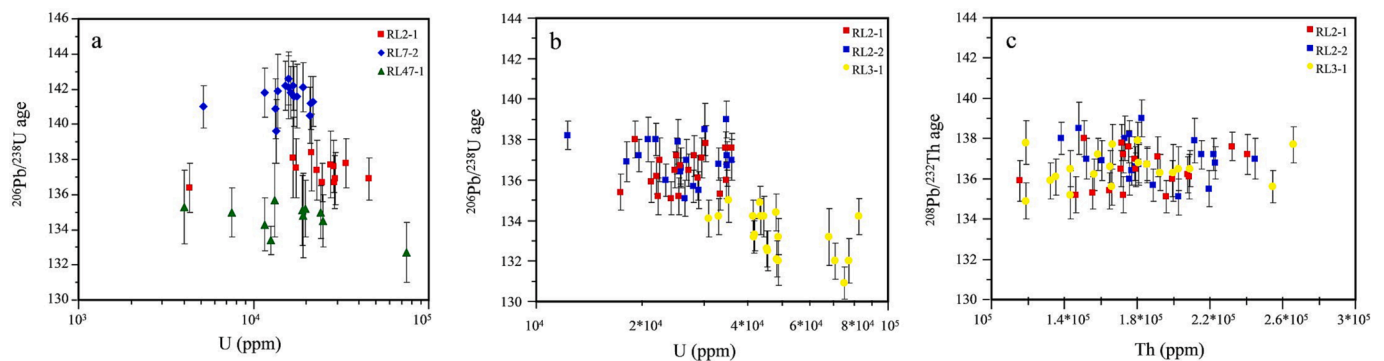
Fig. 9. Zircon $^{206}Pb/^{238}U$ age vs U (a), monazite $^{206}Pb/^{238}U$ age vs U (b), and monazite $^{208}Th/^{232}U$ age vs Th (c) diagrams of the Renli Nos. 2, 3, 7 and 47 pegmatites.

respectively (Li et al., 2019, 2020b; Wang et al., 2014b; Xiong et al., 2020). However, the disparate Hf and Nd isotope compositions do not support the genetic relationship between the intermediate rock and acid rock (Wang et al., 2014b). The prolonged magma activity from the Mufushan granite sequence (154–140 Ma) to the Renli pegmatite sequence (141.5–130.8 Ma) (Table 5; Fig. 10) supports a closely temporal relationship between them. In addition, Nos. 2, 7, and 47

pegmatites have consistent zircon Hf isotope compositions (this work) with the Mufushan BMG and TMG (Li et al., 2020a, b), with εHf (t) values and two-stage model ages (T_{DM2}) in ranges of − 10 to − 5 (Table 3; Fig. 11b, c) and 1.5–1.8 Ga (Table 3; Fig. 11d), respectively, indicating a source connection.

However, the parental granite of the Renli pegmatites remains controversial. For example, Li (2016) suggested that the BMG is the

Table 5

The age statistics on igneous rocks from Mufushan area, South China.

Sample number	Lithology	Type	Age (Ma)	Dating method	Note	Reference
18RL-28	Pegmatite	Nb-Ta	140.2 ± 0.95	coltan U-Pb	No. 5	Xiong et al., 2020
18RL-8		Nb-Ta	140.7 ± 0.50	Monazite U-Pb	No. 5	
MRLm-4		Be-Nb-Ta	125.0 ± 1.40	Ar-Ar	No. 5	Li et al., 2019
RLN1-6		Nb-Ta	133.0 ± 2.60	coltan U-Pb		Li et al., 2020b
RL5		Nb-Ta	131.2 ± 2.40	zircon U-Pb	No. 5	
ZK1616-M1-4		Nb-Ta	130.1 ± 1.1	Re-Os	No. 5	Zhou et al., 2020
H17		Li	130.8 ± 0.9	Ar-Ar	No. 106	Liu et al., 2019
RL7-2		Barren	141.5 ± 0.8	zircon U-Pb	No. 7	This work
RL2-2		Nb-Ta	137.1 ± 0.8	zircon U-Pb	No. 2	
RL2-1		Nb-Ta	136.5 ± 0.4	Monazite U-Pb	No. 2	
RL2-2		Nb-Ta	137.0 ± 0.5	Monazite U-Pb	No. 2	
RL3-1		Nb-Ta	136.5 ± 0.4	Monazite U-Pb	No. 3	
RL47-1		Li	134.5 ± 0.8	zircon U-Pb	No. 47	
PJ-9–7-4		Be	130.5 ± 0.90	Ar-Ar	Daxing	Li et al., 2017
DFS3-3		Nb-Ta	127.7 ± 0.90	Ar-Ar	Duanfengshan	
07MFS25-2	Diorite	Diorite	154.0 ± 1.9	zircon U-Pb		Wang et al., 2014a
07MFS13-1	Granodiorite	Granodiorite	151.5 ± 1.3	zircon U-Pb		
07MFS01-1	Granite	Biotite monzogranite	148.3 ± 1.4	zircon U-Pb		
07MFS18-1		TW leucogranite	145.8 ± 0.9	zircon U-Pb		
QD49		Two-mica monzogranite	131.8 ± 1.5	zircon U-Pb		Ji et al., 2017
H16			141.0 ± 1.2	zircon U-Pb		Liu et al., 2019
RLG-2			138.3 ± 0.3	zircon U-Pb		Li et al., 2020b
RLG-3		Prophyritic biotite monzogranite	140.7 ± 0.7	zircon U-Pb		
RLG-4		Biotite monzogranite	140.3 ± 0.7	zircon U-Pb		
CQSK			142.9 ± 0.9	zircon U-Pb		Xu et al., 2019a,b
18RL-26			154.1 ± 0.98	zircon U-Pb		Xiong et al., 2020
18RL-10		Muscovite Monzogranite	141.0 ± 1.2	zircon U-Pb		
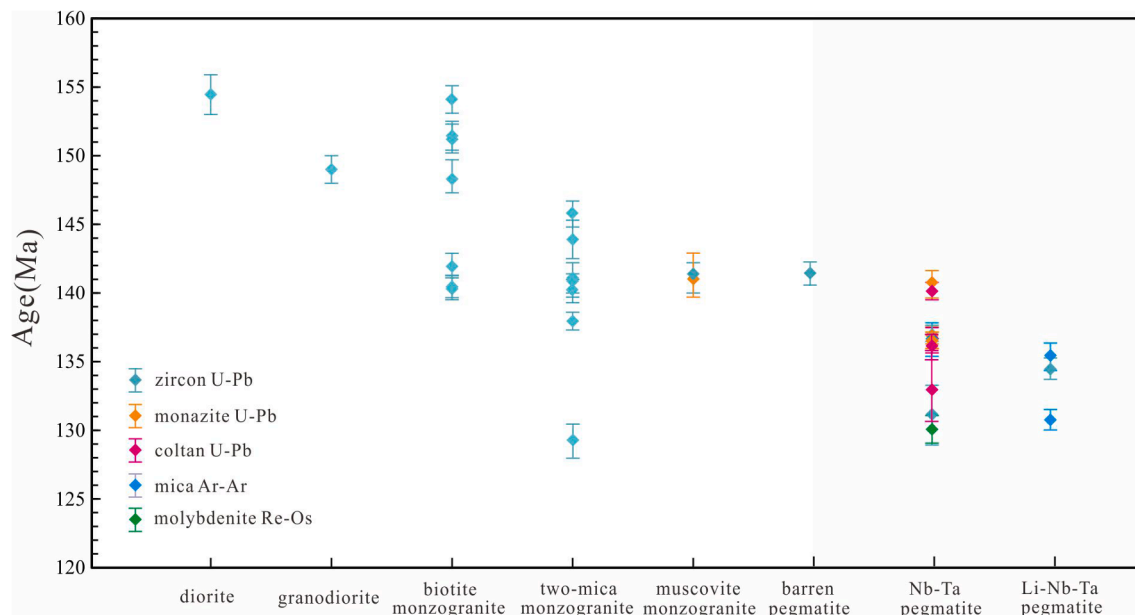
Fig. 10. Statistics on geochronological method and ages of the Mesozoic YMB and Renli rare-metal pegmatites, showing the time sequence of igneous rocks in the Mufushan area.

parental granite of type II pegmatite with Nb–Ta mineralization based on the locally spatial relationship between them. Xiong et al. (2020) hold that the Nb–Ta-mineralized pegmatite is genetically related to MMG rather than BMG according to the temporal-spatial relationship between them and the whole rock chemical compositions of the monzogranites. Li et al. (2021) have recently amended their previous proposal and suggested the closest petrogenetic relationship of TMG with the Renli rare-metal pegmatites based on the geochemical characteristics of muscovites from different types of pegmatites and granites in the Renli mining area.

From the classical model of LCT pegmatite (Černý, 1991; Shearer et al., 1992), the most fractionated granitic phase in a common granite

sequence (such as muscovite granite) is directly responsible for the origin of pegmatites exposed in the same regional zoning (Fig. 12a). However, the petrogenesis of the Renli pegmatite is difficult to explain using this model. First, the MMG shows a small quantity and limited scale and occurs as dikes in BMG (Wang et al., 2014b; Xiong et al., 2020), thus, it is difficult to provide abundant source materials for numerous pegmatites and sufficient Nb, Ta, and Li ore-forming elements for type II and III pegmatites, respectively. Moreover, the deep-buried majority of the MMG can be excluded because of the wide exposure of the lower phases (biotite granite and two-mica granite), indicating a high-level denudation of the YMB. Second, type I pegmatite generally occurs as veins and schlierens in the BMG (Fig. 3e) with a gradual
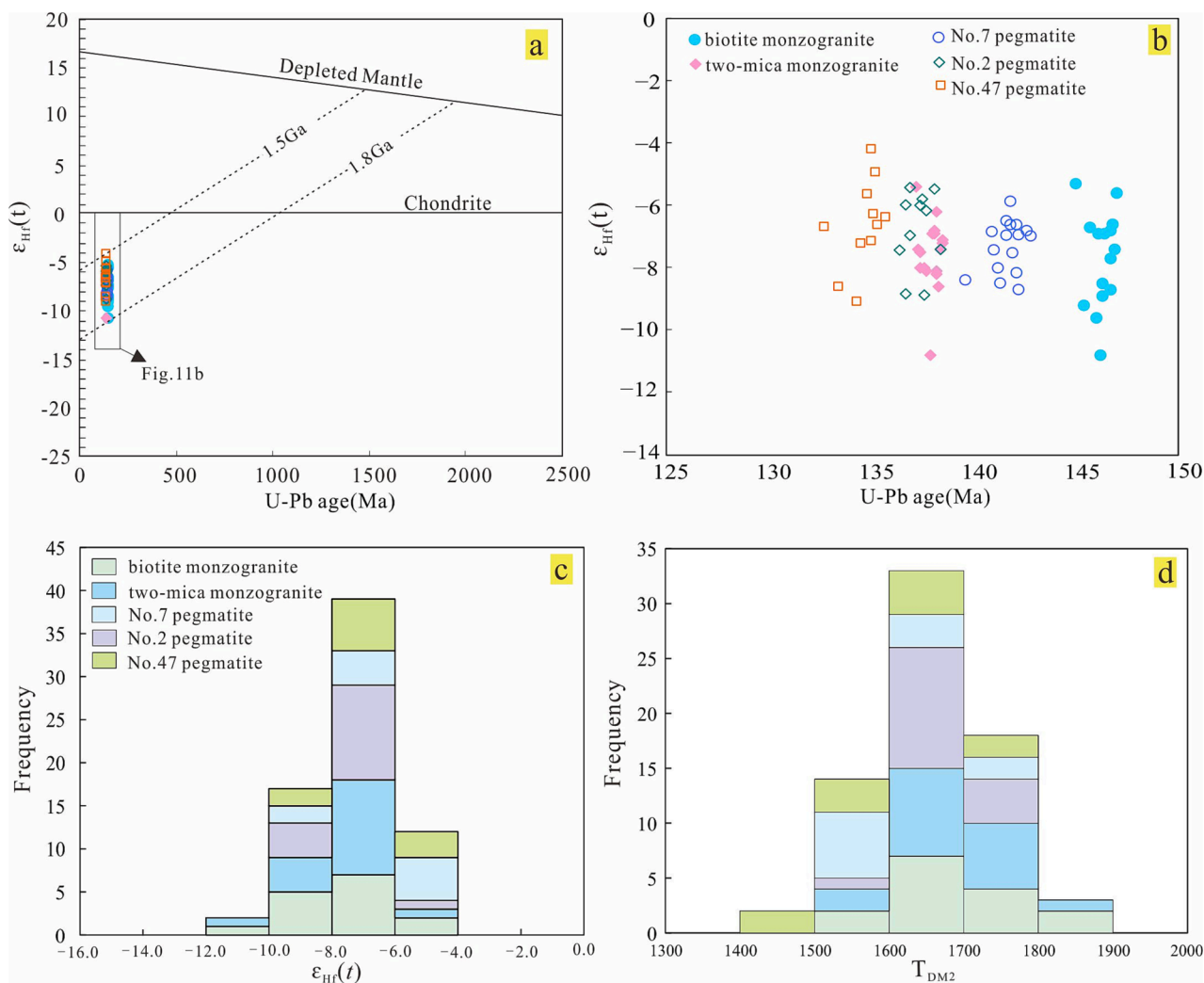
Fig. 11. Zircon $\varepsilon_{Hf}(t)$ vs U–Pb age diagram (a, b). Histogram of zircon $\varepsilon_{Hf}(t)$ values(c). Histogram of zircon Hf-isotope crust model age(T_{DM2}) (d). Zircon data of BMG and TMG are from Li et al. (2020a), Li et al. (2020b).

contact, and the ore-forming mineral of biotite in the BMG is absent in the MMG, indicating a sharp composition discontinuity. Third, no pegmatite regional zoning around the MMG in the Renli mining area and the periphery or interior of the Mufushan batholith is observed. Moreover, the possibility that all three types of pegmatites commonly sourced from the BMG can be excluded based on the following: (1) the occurrence of three phases of granite and three types of pegmatite indicates that fractional crystallization is the dominating mechanism for their formations. Further, it is impossible that, in this case, the type III pegmatite (muscovite–albite–spodumene pegmatite) originates from the BMG owing to a large composition gap between them; (2) the type I pegmatite hosted in the BMG evidently differs to the type II pegmatite hosted in the TMG in mineral assemblage and mineralization (e.g., the former is barren and contains a certain amount of biotite which is absent in the latter). Further, both types occur as schlierens, veins, branches, and pods in the BMG and TMG, without oriented distribution controlled by faults or joints, Further, there is no development of the chill border in the contact zone (Fig. 3a, b). All these evidences support the cogenetic relationship between the type I pegmatite and BMG and the type II and TMG. Accordingly, it is not possible that the type I pegmatite was sourced from a deep-buried biotite granite instead of the exposed BMG. The temporal–spatial and source relationships between the BMG and the type I pegmatite are confirmed herein; however, the occurrence of deep biotite granites in the Mufushan area is also denied by the geophysical study (Ji et al., 2018). Importantly, no other buried granitoids has been

found in the depth of 15 km at least according to the forward gravity modeling along two trending profiles across the Dayunshan-Mufushan batholiths (Ji et al., 2018). With consideration of the effective derive distance of pegmatite from source granites (<10 km), it is meaningless for the pegmatites even if deep granites do exist with bury depth over 15 km.

Although lack of the physical connection of the type III pegmatite with specific granite, the type III pegmatite is close to the MMG in composition (similar rock-forming minerals of albite, quartz and muscovite) and formation age (ca. 135 Ma and 141 Ma, respectively; Table 5). In addition, an exposure of MMG has been demonstrated in Huangboshan area. The MMG has U-Pb age of 141 Ma (Xiong et al., 2020) and is close to the No.47 spodumene-rich pegmatite (no>1 km, Fig. 2), indicating a close temporal-spatial connection between them. More importantly, previous works demonstrated that the BMG and TMG belong to different batches of granitic intrusion rather than the crystallization differentiation production of the same one batch of magma (Ji et al., 2018). The occurrence of MMG dyke in the BMG and TMG also supports that the MMG was the latest intrusion. Therefore, its reasonable that the majority of the MMG could be sealed in the early BMG and TMG or covered by Neoproterozoic sedimentary rocks due to its limited volume.

The BMG exposed in the Renli area was dated at 154.1 ± 2.5 Ma (Xiong et al., 2020) and 140.7 ± 0.7 Ma (Li et al., 2020a), and BMG host type I pegmatite in adjacent area of Renli was dated at 142.9 ± 0.9 Ma
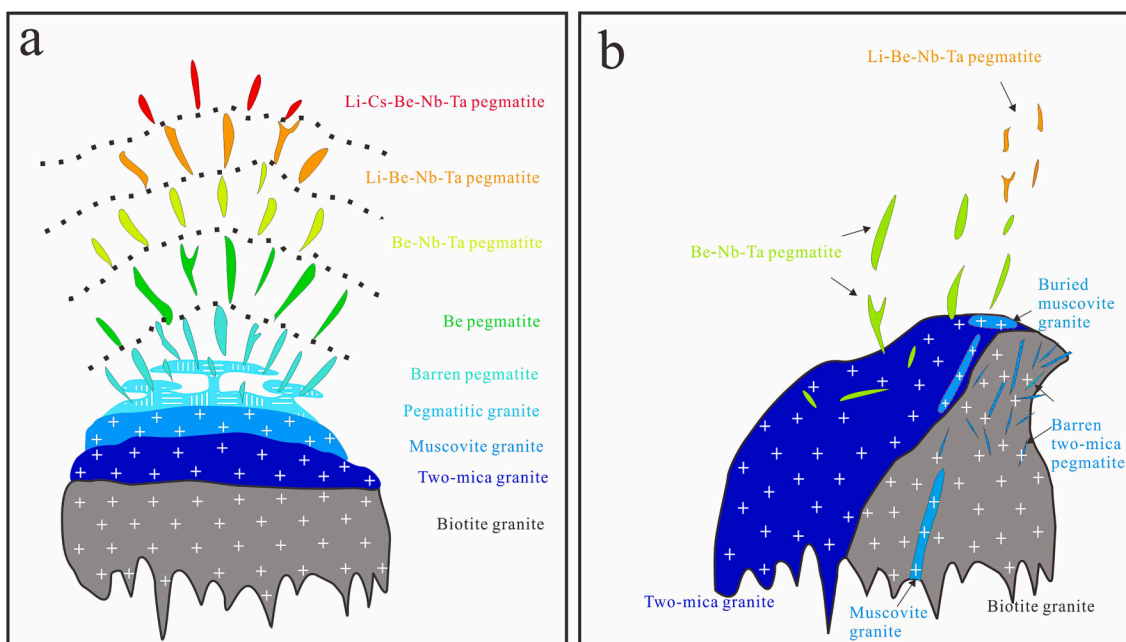
Fig. 12. Classical model for LCT pegmatite (a) (after Černý, 1991; Shearer et al., 1992) and a schematic model for Renli LCT pegmatites (b).

(Xu et al., 2019a,b), the latter two ages coincide with the U–Pb age of the No. 7 pegmatite (141.5 ± 0.8 Ma, this work) within range of error, indicating a temporal relationship. Moreover, the No. 7 pegmatite shows a similar zircon Hf isotope composition to the BMG (Fig. 11), indicating a source connection. Although the TMG shows similar U–Pb ages (141–138 Ma, Li et al., 2020b; Liu et al., 2019) and Hf isotope composition to the type I pegmatite (Fig. 11), it is excluded to be the parental rock of the latter because the type I pegmatite commonly occurs in the BMG as schlieren or vein, with a gradual contact, and it is almost absent in the TMG, indicating a close spatial connection of the type I pegmatite with the BMG. Importantly, the type I pegmatite has primitive components (higher K/Rb and Nb/Ta ratios and lower Li, Rb, and Cs contents) compared to the TMG from a previous study (Li et al., 2021).

The Nos. 2 and 3 pegmatites have zircon and monazite U–Th–Pb ages of 137.1 –136.5 Ma, and the No. 47 pegmatite was formed at ~ 134.5 Ma (Figs. 7, 8), which are slightly younger than the ages of the TMG (141–138.3 Ma, Li et al., 2020b; Liu et al., 2019). The TMG occupies a large proportion of the Mufushan batholith and hosts plenty of Be and Be–Nb–Ta-mineralized pegmatites, i.e., the type II, (Fig. 1). Similar to the type I pegmatite, the type II pegmatite occurs as veins and schlierens in the TMG with gradual contacts between them (Fig. 3b). Moreover, the studied types II pegmatite has consistent zircon Hf isotope compositions with the TMG (Fig. 11). The above mentioned evidence supports that the TMG could be the parental rock of types II pegmatite in the Renli mining area.

Hence, we propose a new parallel differentiation model for the generation of the Renli LCT pegmatites, i.e., the types I, II and III pegmatites were derived from the BMG, TMG and MMG, (Fig. 12b), respectively. In Black Hills, South Dakata, USA, plenty of pegmatites distributed in/around the Harney Peak Granite. Three trajectories of fractional crystallization were identified after analyzing a mass of composition data of potash feldspar from pegmatite and granite samples (Shearer, 1992). Except the pegmatites sharing a same trajectory of fractional crystallization with the Harney Peak Granite, the Li-, Rb-, Cs-enriched zoned pegmatites and F-, sn-, Be-enriched pegmatites show distinct differentiation trajectories to any specific granites. They could be formed by anatexis rather than fractional crystallization of granitic melts (Shearer, 1992). Although the pegmatites from Renli and Black Hills both have various origins and types, but they are essentially different in source. The types I, II, and III pegmatites from Renli have a common source indicated by their consistent Hf isotope compositions (Fig. 11b). In contrast, the three pegmatite arrays, i.e., the Harney Peak Granite-related pegmatites, Li-, Rb-, Cs-enriched zoned pegmatites and F-, sn-, Be-enriched pegmatites from Black Hills were derived from distinct sources (Shearer, 1992). In a nutshell, the differences among pegmatites in Renli resulted from the level of fractional crystallization of a common melt, and for the pegmatites from Black Hills, source and partial melting degree are dominating factors.

It is still unclear what factors control the differentiation of granitic melts, however, the differentiation mechanism considerably restricts the spatial relationship between pegmatite and parental granite. If crystal-melt fractionation was the dominating way, the interior residual melts were hard to accumulate and migrate adequately. Therefore, they were hard to extract from the source magma (Černý, 1991). Pegmatites originating from these melts are generally emplaced in their source rocks, such as the type I pegmatite in Renli. If melt fractionation was controlled by filter pressing and gravity convection–diffusion, the residual melts were inclined to accumulate in the uppermost domes of source melt (Černý, 1991), and emplaced commonly out of their parental rocks owing to low viscosity and sudden extractions promoted by the enrichment of volatiles and pressure variations, respectively, such as the type III pegmatite.

7.3. Source of the Renli pegmatite

Zircon has been used effectively as a proxy for tracing crust–mantle evolution by the combination of its U–Pb age and Hf isotope composition (Amelin et al., 1999; Griffin et al., 2002; Scharer et al., 1997). Zircons formed in pegmatites, especially those having rare-metal mineralizations, are commonly rich in Hf and transform to hafnon sometimes. High Hf content in pegmatite-forming melt endows the authority on provenance identification by Hf isotopes. It has been demonstrated that metamictization, recrystallization, and metasomatism hardly modify the original Hf isotope composition of zircon from highly differentiated pegmatite (Chen et al., 2018; Lv et al., 2012; Tang et al., 2017). Monazite is a common mineral and widely applied in chronology and isotope studies because of the Th, U, and light rare earth element enrichment and the high closure temperatures of U–Pb and Sm–Nd isotope systems (e.g., Cottle et al., 2019; Fisher et al., 2020; Liu et al., 2012; Pandur et al., 2020; Pearce et al., 1999).

Zircons from the Nos. 2, 7, and 47 pegmatites have almost the same Hf isotope composition, also coincident with those of the BMG (Li et al., 2020a) and TMG (Li et al., 2020b) in the Renli area (Fig. 9). The pegmatites show $\varepsilon_{Hf}(t)$ values − 10 to − 5 (Table 3; Fig. 9b, c) and T_{DM2} of 1.5–1.8 Ga (Table 3; Fig. 9d). Monazites from the Nos. 2 and 3
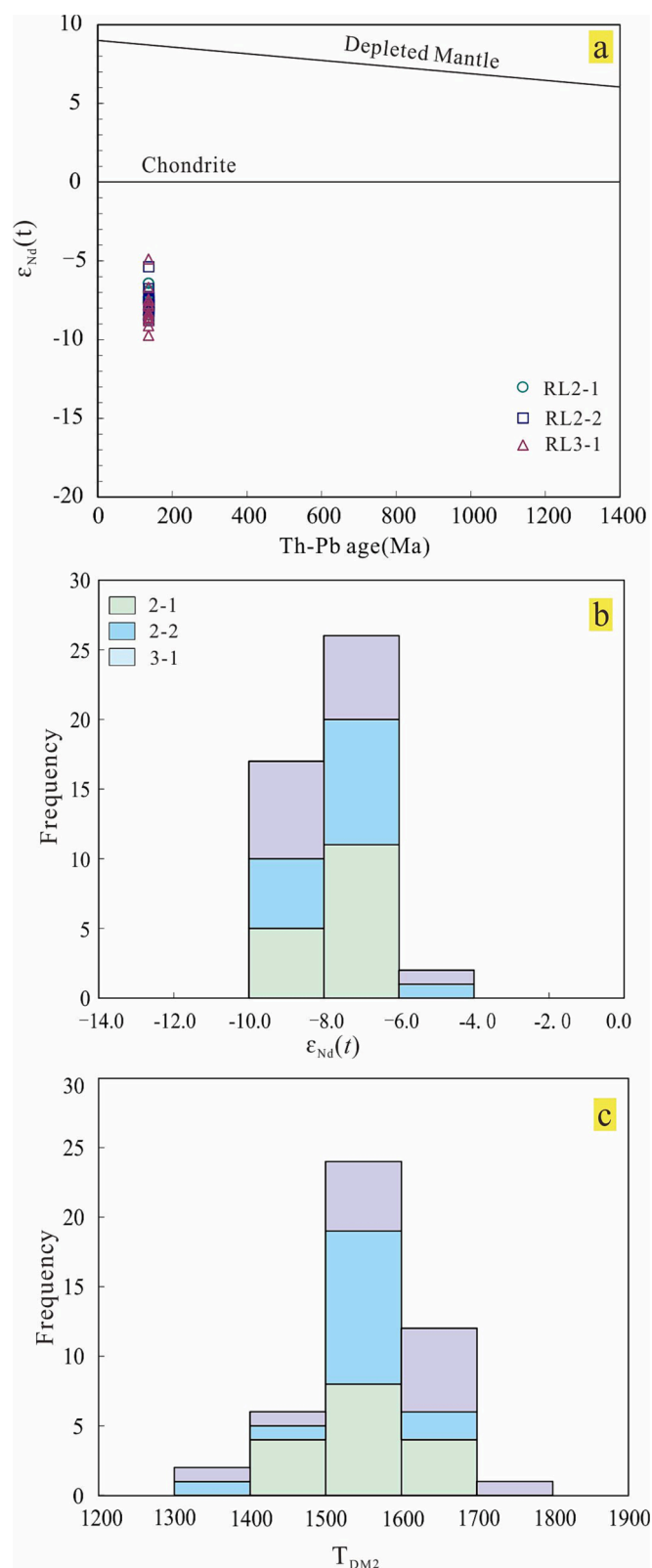
pegmatites in the Renli area have negative $\varepsilon_{Nd}(t)$ values (Table 4; Fig. 13a), with>90 % of the data in the range of − 10 and − 6 (Table 4; Fig. 13b), and the T_{DM2} of 1.4–1.7 Ga (Table 4; Fig. 13c), consistent with the zircon Hf isotope compositions of $\varepsilon_{Hf}(t)$ (−10 to − 5) and T_{DM2} (1.5–1.8 Ga) mentioned above. The monazites from the RL2-1 sample show $\varepsilon_{Nd}(t)$ values of − 6.42 to − 8.77 (Table 4), with corresponding $\varepsilon_{Hf}(t)$ values of − 5.78 to − 8.97 based on the conversion formula by Vervoort et al. (1999). These values are consistent with the $\varepsilon_{Hf}(t)$ values (−4.85 to − 8.87, Table 3) of zircons from the RL2-1 sample, indicating the coupled Nd–Hf isotope compositions of the Renli pegmatites.

The JOB is a Neoproterozoic convergent orogen formed by Yangtze and Cathaysia block amalgamation (e.g., Wang et al., 2014a, 2017b; Zhou et al., 2009). Although a large number of granites were generated during orogenesis, only the Fanjingshan granite contributed to pegmatite formation and rare-metal mineralization in the western JOB. A systematic study of pegmatite, granite, and sedimentary rocks demonstrated that the Fanjingshan granite–pegmatite suite has Sn–Nb–Ta mineralization and originates from the partial melting of sedimentary rocks from the Fanjingshan Group at ca.830 Ma (Lv et al., 2021a). The Lengjiaxi Group exposed in the Renli area (Figs. 1 and 2) has a similar maximum deposit age (ca. 860–820 Ma) to the Fanjingshan Group and contemporaneous strata in the JOB (e.g., the Shuangqiaoshan Group in Jiangxi and the Sibao Group in Guangxi). They were formed by deposition in a backarc setting with varying sources from eastern to western JOB (e.g., Wang et al., 2014a, 2017b)and are regarded as the major source of Neoproterozoic granites (e.g., Li et al., 2003; Wu et al., 2006a, b; Zheng et al., 2007).

Compared to the Neoproterozoic Fanjingshan rare-metal granite–pegmatite suite ($\varepsilon_{Hf}(t)$ = +1.13 − −9.51, T_{DM2} = 2.31–1.65 Ga, Lv et al., 2021a), the Renli granite and pegmatite have relatively depleted zircon Hf isotope composition ($\varepsilon_{Hf}(t)$ = -3.0 − −10.8 T_{DM2} = 1.88–1.39 Ga, Fig. 14), indicating the contribution of more juvenile crust materials to the Renli granite and pegmatite. However, they totally match with the Neoproterozoic granitoids exposed in northeastern Hunan (Figs. 14 and 15) in zircon Hf isotope compositions, indicating their common source. Although the younger (T_{DM2} < 1.2 Ga) and older (T_{DM2} > 2.0 Ga) components of the Lengjiaxi Group are absent in the Renli granite and pegmatite according to the statistics of comparison of model age (Fig. 15), the Renli granite and pegmatite could be sourced from the sedimentary rocks of Lengjiaxi Group. Because a few of inherited zircons have been observed in the BMG and TMG of the YMB with dominating ages of 700–900 Ma (Li et al., 2020b; Wang et al., 2014b; Xiong et al., 2020), and these zircon U-Pb ages are totally consistent with the dominating age of detrital zircons (690–950 Ma, Li et al., 2020b) from the Lengjiaxi Group, indicating a strong source connection of the Mesozoic granite-pegmatite suite with the Neoproterozoic sedimentary rocks.

In conclusion, the Renli LCT pegmatites and their parental granites originate from the partial melting of the sedimentary rocks from the Neoproterozoic JOB.

7.4. Petrogenetic and mineralization model of the Renli pegmatite

Based on the distribution location of pegmatite worldwide, Dill (2015, 2016) summarized five types of geodynamic settings for pegmatite formation, namely, Alpine, Variscan, Rift, Andean, and island arc. Among them, the Variscan type orogen setting is the uppermost for pegmatite formation because of the largely thickened crust. A thinned crust and alkaline magmatism characterize the Rift setting (Dill, 2015), indicating a facilitated setting for Nb-, Y-, and F-rich pegmatite (Černý, 1991). In comparison, the Andean and island arc settings are averse to pegmatite formation, and pegmatites are generally formed in hinterland far away from the active continental margin (Dill, 2016). The Mesozoic geology of South China is different from that of the Andean subduction setting and Japan Island Arc (e.g., Mao et al., 2014). Tectonic studies
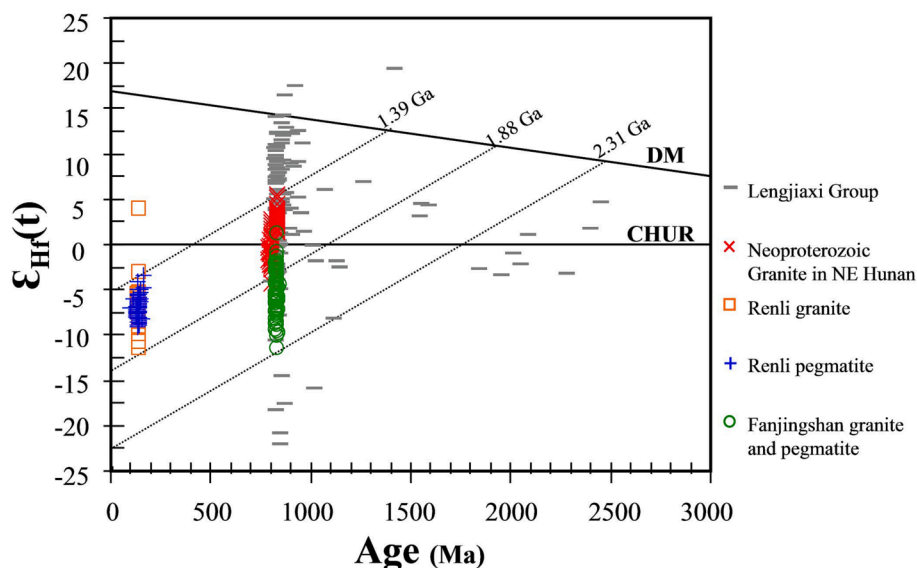
Fig. 13. Monazite $\varepsilon_{Nd}(t)$ vs Th–Pb age diagram(a). Histogram of monazite εNd (t) values(b). Histogram of monazite Nd-isotope crust model age (T_{DM2}) (c).

Fig. 14. Diagram of ε$_{Hf}$(t) value vs crystallization ages of detrital and igneous zircons from the JOB. Data of zircon are from Li et al. (2020b), Lv et al. (2021a), Wang et al. (2011), Wang et al. (2014a), and this work.
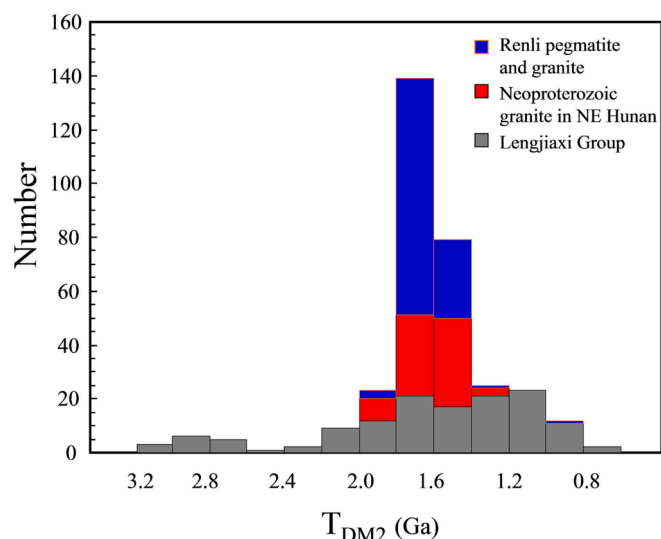

Fig. 15. Histogram of zircon Hf-isotope crust model age (T$_{DM2}$) of pegmatite, granite and schist from the Mufushan area and northeastern Hunan. Data of the Lengjiaxi Group from Wang et al. (2016) and Li et al. (2020a), , Li et al. (2020b); data of the Neoproterozoic granite from Ma et al.(2009) and Wang et al. (2014a); data of Renli pegmatite and granite from Li et al. (2020a, , Li et al. (2020b) and this work.

have indicated that the Mufushan granite and pegmatite might be formed in (1) a postorogenic setting after the early Triassic collision between South China and North China blocks (Li et al., 1993; Zhou et al., 2006), or (2) a *syn*-orogenic subduction setting induced by the subduction of the paleo-Pacific Ocean plate under the South China block (Li and Li, 2007; Jiang et al., 2009; Sun et al., 2012). However, the second setting is preferentially considered here owing to the face that (1) the activities of the Mufushan granite and pegmatite largely lag behind the postorogenic granites formed at 243–214 Ma after collision (e.g., Wang et al., 2007) and (2) the Middle Jurassic–Early Certaceous granites and related rare metal ore deposits mainly concentrate in the South China block (e.g., Wang et al., 2014b). Further, they show a NE-striking distribution vertical to the northwestward subduction. Although the syn-–orogenic stage is commonly characterized by extrusion stress and

thickened crust compressional setting, an extension setting is preferentially considered for the Mufushan granite and pegmatite during the Late-Jurassic to Early Cretaceous, according to the following. (1) the bimodal magmatic suites comprise gabbro and granite that have been confirmed in Mufushan area (Wang et al., 2014b; Chen et al., 2021), and the juxtaposing of gabbro and granite generally indicates extensional settings (Bonin, 2004; Pin and Paquette, 1997; Tang et al., 2013); (2) the pervasive Mesozoic granitoids and volcanic rocks in South China have been attributed to the production of lithospheric extension caused by the roll back of the paleo-Pacific Ocean plate (Zhou et al., 2006; Li and Li, 2007), especially for the Late Jurassic to the Early Cretaceous granitoids exposed in Mufushan and Lianyunshan (Wang et al., 2014; Wang et al., 2016; Ji et al., 2017). In addition, the Late Jurassic to Early Cretaceous lithospheric extension also promoted the generations of the Pb–Zn, W, and other rare-metal ore deposits in South China (Shu et al., 2021; Yu et al., 2020; Zhao et al., 2017). Combined with previous studies, we propose the following geodynamic scenario for the YMB during the early Yanshanian:

Lithospheric extension and intense magmatism in South China have been caused by the long-distance subduction the paleo-Pacific plate in the Late Jurassic to the Early Cretaceous (e.g., Li and Li, 2007; Shu et al., 2021). In the Mufushan area, the underplating of mantle magma causes the generation of high-Mg diorite at ca. 154 Ma and a large volume of granitic magma derived by the partial melting of the JOB crust at ca. 148 Ma (Wang et al., 2014b). The initial granite-forming melts of the BMG, TMG, and MMG were successively formed by the sufficient crystallization differentiation of the granitic magma because of the extended heat supply from the prolonged mantle magmatisms (154–137 Ma, Chen et al., 2021; Wang et al., 2014b). Meanwhile, the types I, II and III pegmatite-forming melts were derived by crystallization differentiation of the BMG, TMG and MMG melts, respectively. The type I melt had hardly escaped from its parental melt owing to the evident lack of volatile components. However, the types II and III pegmatite-forming melts were extracted from their parental magma and mostly emplaced in peripheral sedimentary rocks, i.e., the Lengjiaxi Group (Figs. 2, 12b).

Comparatively, *syn*-orogenic LCT pegmatites are rarer than those formed in the postorogenic extension setting (Černý, 1991; Lv et al., 2018). In the Chinese Altai, the Devonian *syn*-orogenic pegmatite was formed by the partial melting of Early Paleozoic accreted materials in a fore-arc extension setting caused by the subduction of the ocean ridge and the upwelling of the asthenosphere mantle (Lv et al., 2018), accompanied by with coeval high temperature metamorphism (e.g.,

720 °C–650 °C). Conversely, the Mufushan pegmatites were formed in inland far away from the active continental margin, and sourced from the backarc sedimentary materials accreted in the Neoproterozoic Jiangnan orogeny rather than the newly accreted materials during the subduction of paleo-Pacific Ocean. The specific reasons caused in these discrepancies are still unclear and need to be studied in the future. The prolonged heat supply may be critical to the differentiation of the rare-metal granite–pegmatite suite formed in a subduction setting. Moreover, the source inherited from ancient orogen and further enrichment of rare-metal elements caused by the cycling of ancient orogenic crust may contribute to the mineralization of the inland synorogenic peraluminous magmas. These factors may explain the barren property of the Neo-proterozoic granites in Northeast Hunan Province although they have the same source as the YMB from the sedimentary rocks of the Lengjiaxi Group. However, future work on the migration and enrichment mechanisms of rare-metal elements during crust reworking and cycling should be done.

8. Conclusions

(1) The results of zircon U–Pb and monazite U–Th–Pb dating reveal that the Renli biotite–muscovite–microline pegmatite (type I) was formed at ca. 141 Ma, muscovite–microcline–albite pegmatite(type II) at ca. 137 Ma, and albite–spodumene pegmatite(type III) at ca. 134 Ma, with decreasing ages from the barren pegmatite to the Li mineralization pegmatite.

(2) The biotite–muscovite–microline pegmatite (type I) originates from the BMG, while the muscovite–microcline–albite pegmatite (types II) and albite–spodumene pegmatite (type III) may originate from the TMG and MMG, respectively, indicating a new petrogenesis model of parallel differentiations of triple source granitic melts for the LCT pegmatites in South China.

(3) The Renli LCT pegmatites have coupled Hf–Nd isotope compositions with model ages of 1.4–1.8 Ga, and the Hf isotope compositions are similar to that of the Neoproterozoic granitoids and match with the sedimentary rocks from the Neoproterozoic Lengjiaxi Group, indicating that the Renli LCT pegmatites originated from the reworking materials of the Neoproterozoic JOB.

Declaration of Competing Interest

The authors declare that they have no known competing financial interests or personal relationships that could have appeared to influence the work reported in this paper.

Data availability

Data will be made available on request.

Acknowledgments

References

Amelin, Y., Lee, D.C., Halliday, A.N., Pidgeon, R.T., 1999. Nature of the Earth's earliest crust from hafnium isotopes in single detrital zircons. Nature 399, 252–255.

Ayers, J.C., Dunkle, S., Gao, S., Miller, C.F., 2002. Constraints on timing of peak and retrograde metamorphism in the Dabie Shan Ultrahigh-pressure Metamorphic Belt, east-Central China, using U-Th–Pb dating of zircon and monazite. Chem. Geol. 186, 315–331.

Barros, R., Menuge, J.F., 2016. The origin of spodumene pegmatites associated with the Leinster granite in Southeast Ireland. Can. Mineral. 54, 847–862.

Blichert-Toft, J., Albarède, F., 1997. The Lu-Hf isotope geochemistry of chondrites and the evolution of the mantle–crust system. Earth Planet. Sc. Lett. 148, 243–258.

Bonin, B., 2004. Do coeval mafic and felsic magmas in post-collisional to within-plate regimes necessarily imply two contrasting, mantle and crustal, sources? A review. Lithos 78, 1–24.

Cawood, P.A., Wang, Y., Xu, Y., Zhao, G., 2013. Locating South China in Rodinia and Gonwana: a fragment of greater India lithosphere? Geology 41, 903–906.

Černý, P., 1991. Rare element granitic pegmatites. Part II: Regional and global environments and petrogenesis. Geosci. Can. 18, 68–81.

Černý, P., Ercit, T.S., 2005. The classification of granitic pegmatites revisited. The Can. Mineral. 43, 2005–2026.

Černý, P., London, D., Novak, M., 2012. Granitic pegmatites as reflections of their sources. Elements 8, 289–294.

Chen, J.F., Zhang, H., Zhang, J.X., Ma, Y.H., 2018. Geochronology and Hf isotope of zircon for Koktokay No.3 granitic pegmatite in Xinjiang and its geological implications. China J. Nonfer. Metal. 28, 1832–1845 in Chinese with English abstract.

Chen, J.F., Wen, C.H., Huang, J.Z., Zhang, J.X., Wang, C., Tang, Y., Lv, Z.H., Zhou, F.C., Cao, C.H., Chen, Y.P., 2021. Characteristics of No.7 pegmatite and pyroxene diorite in Renli rare metal deposit, south margin of Mufushan batholiths and its geological implications. Geotec. Metal. 10 (5), 951–967 in Chinese with English abstract.

Cherniak, D.J., Watson, E.B., 2000. Pb diffusion in zircon. Chem. Geol. 172, 5–24.

Chu, N.C., Taylor, R.N., Chavagnac, V., Nesbitt, R.W., Boella, R.M., Milton, J.A., Burton, K., 2002. Hf isotope ratio analysis using multi-collector inductively coupled plasma mass spectrometry: An evaluation of isobaric interference corrections. J. Anal. Atom. Spectrom 17, 1567–1574.

Cottle, J., Lederer, G., Larson, K., 2019. The monazite record of pluton assembly: Mapping manaslu using Petrochronology. Chem. Geol. 530, 119309.

Cottle, J.M., Searle, M.P., Jessup, M.J., Crowley, J.L., Law, R.D., 2015. Rongbuk re-visited: Geochronology of leucogranites in the footwall of the South Tibetan Detachment System, Everest Region, Southern Tibet. Lithos 227, 94–106.

Deng, T., Xu, D.R., Chi, G.X., Wang, Z.L., Jiao, Q.Q., Ning, J.T., Dong, G.J., Zou, F.H., 2017. Geology, geochronology, geochemistry and ore genesis of the Wangu gold deposit in northeastern Hunan Province, JiangnanOrogen South China. Ore Geol. Rev. 88, 619–637.

Dill, H.G., 2015. Pegmatites and aplites: Their genetic and applied ore geology. Ore Geol. Rev. 69, 417–561.

Dill, H.G., 2016. The CMS classification scheme (Chemical composition-Mineral assemblage-Structural geology)-linking geology to mineralogy of pegmatitic and aplitic rocks. NeuesJahrbuchfürMineralogie-Abhandlungen. J. Mineral. Geochem. 193, 231–263.

Ding, T., Rees, C.E., 1984. The sulphur isotope systematics of the Taolin Lead-zinc ore deposit, China. Geochim. Cosmochim. Acta 48, 2381–2392.

Fisher, C.M., Bauer, A.M., Luo, Y., Sarkar, C., Hanchar, J.M., Vervoort, J.D., Tapster, S.R., Horstwood, M., Pearson, D.G., 2020. Laser ablation split-stream analysis of the Sm-Nd and U-Pb isotope compositions of monazite, titanite, and apatite–Improvements, potential reference materials, and application to the Archean Saglek Block genesis. Chem. Geol. 539, 119493.

Gao, L.Z., Chen, J., Ding, X.Z., Liu, Y.R., Zhang, C.H., Zhang, H., Liu, Y.X., Pang, W.H., Zhang, Y.M., 2011. Zircon SHRIMP U-Pb dating of the tuff bed of Lengjiaxi and Banxi groups, northeastern Hunan: constraints on the Wuling movement. Geol. Bull. China 30, 1001–1008 in Chinese with English abstract.

Goncalves, G.O., Lana, C., Scholz, R., Buick, I., Gerdes, A., Kamo, S.L., Corfu, F., Marinho, M.M., Chaves, A.O., Valeriano, C., Nalini, H.A., 2016. An assessment of monazite from the Itambé pegmatite district for use as U-Pb isotope reference material for microanalysis and implications for the origin of the "Moacyr" monazite. Chem. Geol. 424, 30–50.

Griffin, W.L., Pearson, N.J., Belonsova, E., Jackson, S.E., Achterherah, E.V., O'Reilly, S. Y., Shee, S.R., 2000. The Hf isotope composition of cratonic mantle: LA-MC-ICPMS analysis of zircon megacrysts in kimberlites. Geochim. Cosmochim. Acta 64, 133–147.

Griffin, W.L., Wang, X., Jackson, S.E., Pearson, N.J., O'Reilly, S.Y., Xu, X., Zhou, X., 2002. Zircon chemistry and magma mixing, SE China: In-situ analysis of Hf isotopes, Tonglu and Pingtan igneous complexes. Lithos 61, 237–269.

Griffin, W.L., Pearson, N.J., Belousova, E.A., Saeed, A., 2006. Comment: Hf-isotope heterogeneity in zircon 91500. Chem. Geol. 23, 358–363.

Harrison, T.M., Celerier, J., Aikman, A.B., Herman, J., Heiziler, M.T., 2009. Diffusion of [40]Ar in muscovite. Geochim. Cosmochim. Acta 73, 1039–1051.

Hunan Institute of Geological Survey (HIGS), 2009. 1:250000 Regional Geological Survey Report of Yueyang Area. Hunan Institute of Geological Survey, Changsha, 71 pp. (in Chinese).

Hoskin, P.W.O., Schaltegger, U., 2003. The composition of zircon and igneous and metamorphic petrogenesis. Rev. Mineral. Geochemi. 53, 27–62.

Hu, Z.C., Gao, S., Liu, Y.S., Hu, S.H., Chen, H.H., Yuan, H.L., 2008. Signal enhancement in laser ablation ICP-MS by addition of nitrogen in the central channel gas. J. Anal. Atom. Spectrom 23, 1093–1101.

Hu, Z., Liu, Y., Chen, L., Zhou, L., Li, M., Zong, K., Gao, S., 2011. Contrasting matrix induced elemental fractionation in NIST SRM and rock glasses during laser ablation ICP-MS analysis at high spatial resolution. J. Anal. Atom. Spectrom 26, 425–430.

Hu, A.X., Peng, J.T., 2018. Fluid inclusions and ore precipitation mechanism in the giant Xikuangshan mesothermal antimony deposit, South China: Conventional and infrared microthermometric constraints. Ore Geol. Rev. 95, 49–64.

Isnard, H., Brennetot, R., Caussignac, C., Caussignac, N., Chartier, F., 2005. Investigations for determination of Gd and Sm isotopic compositions in spent nuclear fuels samples by MC ICPMS. Int. J. Mass Spectrom. 246, 66–73.

Ji, W.B., Lin, W., Faure, M., Chen, Y., Xue, Z., 2017. Origin of the Late Jurassic to Early Cretaceous Peraluminous Granitoids in the Northeastern Hunan Province (middle Yangtze Region), South China: Geodynamic Implications for the Paleo-Pacific Subduction. J. Asian Earth Sci. 141, 174–193.

Ji, W.B., Faure, M., Wei, L., Yan, Y., Xue, Z., 2018. Multiple emplacement and exhumation history of the Late Mesozoic Dayunshan-Mufushan batholith in Southeast China and Its tectonic significance: 1. structural analysis and geochronological constraints. J. Geophys. Res-Sol. Ea. 123, 689–710.

Jiang, Y.H., Jiang, S.Y., Dai, B.Z., Liao, S.Y., Zhao, K.D., Ling, H.F., 2009. Middle to Late Jurassic felsic and mafic magmatism in southern Hunan Province, Southeast China: implications for a continental arc to rifting. Lithos 107, 185–204.

Knoll, T., Schuster, R., Huet, B., 2018. Spodumenepegmatites and related leucogranites from the Austroalpine Unit (Eastern Alps, Central Europe): field relations, petrography, geochemistry and geochronology. Can. Mineral. 56, 489–528.

Li, C.Y., 2016. The Genesis of Chuanziyuan Niobium-Tantalum-Lithium Rare Metal Deposit in Pingjiang Hunan: Master Dissertation. Central South Univ. 1–68 in Chinese with English abstract.

Li, X.H., Li, Z.X., Ge, W.C., Zhou, H.W., Li, W.X., Liu, Y., Wingate, M.T.D., 2003. Neoproterozoic granitoids in South China: crustal melting above a mantle plume at ca. 825 Ma? Precamb. Res. 122, 45–83.

Li, Z.X., Li, X.H., 2007. Formation of the 1300 km-wide intracontinental orogen and postorogenic magmatic province in Mesozoic South China: A flat-slab subduction model. Geology 35, 179–182.

Li, X.H., Li, W.X., Li, Z.X., Lo, C.H., Wang, J., Ye, M.F., Yang, Y.H., 2009. Amalgamation between the Yangtze and Cathaysia Blocks in South China: constraints from SHRIMP U-Pb zircon ages, geochemistry and Nd–Hf isotopes of the Shuangxiwu volcanic rocks. Precamb. Res. 174, 117–128.

Li, P., Li, J., Pei, R., Leng, S., Zhang, X., Zhou, F., 2017. Multistage magmatic evolution and cretaceous peak metallogenic epochs of Mufushan composite granite mass: constrains from geochronological evidence. Earth Sci. 42, 1684–1696 in Chinese with English abstract.

Li, P., Liu, X., Li, J.K., Huang, Z.B., Zhou, F.C., Zhang, L.P., 2019. Petrographic and geochemical characteristics of Renli-Chuanziyuan No. 5 pegmatite, NE Hunan, and its metallogenic age. Acta Geol. Sin. 93, 1374–1391 in Chinese with English abstract.

Li, P., Li, J.K., Liu, X., Li, C., Huang, Z.B., Zhou, F.C., 2020b. Geochronology and source of the rare-metal pegmatite in the Mufushan area of the Jiangnan orogenic belt: A case study of the giant Renli Nb–Ta deposit in Hunan, China. Ore Geol. Rev. 116, 103237.

Li, P., Li, J.K., Chen, Z.Y., Liu, X., Huang, Z.B., Zhou, F.C., 2021. Compositional evolution of the muscovite of Renli pegmatite-type rare-metal deposit, northeast Hunan, China: Implications for its petrogenesis and mineralization potential. Ore Geol. Rev. 138, 104380.

Li, X.H., Long, W.H., Li, Q., Liu, Y., Zheng, Y., Yang, Y.H., Chamberlain, K.R., Wan, D.F., Cuo, C.H., Wang, X.C., Tao, H., 2010. Penglai zircon megacrysts: a potential new working reference material for microbeam determination of Hf–O isotopes and U-Pb age. Geostand. Geoanal. Res. 34, 117–134.

Li, L.G., Wang, L.X., Tian, Y., Ma, C.Q., Zhou, F.C., 2018. Petrogenesis and rare-metal mineralization of the Mufushan granitic pegmatite, south China: insights from in situ mineral analysis. Earth Sci. 44, 2532–2550 in Chinese with English abstract.

Li, Q.L., Yang, Y., Liu, Y., Tang, G.Q., Hao, J.L., Zhang, J.C., Hu, S., Zhao, X.C., Chen, Y.L., Chu, X.L., Wang, Y., Jiang, Y., 2013. Ion microprobe microanalytical techniques and their applications in earth science. Bull. Mineral. Petrol. Geochem. 32, 310–327 in Chinese with English abstract.

Li, P., Zhou, F.C., Li, J.K., Liu, X., Huang, Z.B., Zhang, L.P., 2020a. Zircon U-Pb ages and Hf isotopic compositions of the concealed granite of Renli-Chuangziyuan deposit, NE Hunan and geological significance. Geotec. Metal. 44, 486–500 in Chinese with English abstract.

Li, P.C., 2006. Magmatism of Phanerozoic granitoids in southeastern Hunan Province, China and its evolution regularity. Beijing: Chinese Academy of Geological Sciences (doctoral dissertation), 35–44 (in Chinese with English abstract).

Liu, Y.S., Gao, S., Hu, Z.C., Gao, C.G., Zong, K., Wang, D., 2010a. Continental and oceanic crust recycling-induced melt–peridotite interactions in the trans-North China orogen: U-Pb dating, Hf isotopes and trace elements in zircons from mantle xenoliths. J. Petrol. 51, 537–571.

Liu, Y.S., Hu, Z.C., Zong, K.Q., Gao, C.G., Gao, S., Xu, J., Chen, H.H., 2010b. Reappraisement and refinement of zircon U-Pb isotope and trace element analyses by LA-ICP-MS. Chinese Sci. Bull. 55, 1535–1546 in Chinese with English abstract.

Liu, Z.C., Wu, F.Y., Yang, Y.H., Yang, J.H., Wilde, S.A., 2012. Neodymium isotopic compositions of the standard monazites used in U-Th-Pb geochronology. Chem. Geol. 334, 221–239.

Liu, X., Zhou, F.C., Li, P., Li, J.K., Huang, Z.B., Shi, W.K., Hunag, X.Q., Zhang, L.P., Su, J.N., 2019. Geological characteristics and metallogenic age of Renli rare metal orefield in Hunan and its prospecting significance. Miner. Depos. 38, 771–791 in Chinese with English abstract.

London, D., 2014. A petrologic assessment of internal zonation in granitic pegmatites. Lithos 184, 74–104.

London, D., 2018. Ore-forming processes within granitic pegmatites. Ore Geol. Rev. 101, 349–383.

London, D., Hunt, L., Schwing, C.R., Guttery, B.M., 2020. Feldspar thermometry in pegmatites: truth and consequences. Contrib. Mineral. Petr. 175, 8.

Ludwig, K.R., 2011. Isoplot v. 4. 15: A Geochronological Toolkit for Microsoft Exce. Berkely: Berkeley Geochronology Center Special Publication, 1–75.

Lv, Z.H., Zhang, H., Tang, Y., Guan, S.J., 2012. Petrogenesis and magmatic–hydrothermal evolution time limitation of Kelumute no. 112 pegmatite in Altay, Northwestern China: evidence from zircon U-Pb and Hf isotopes. Lithos 154, 374–391.

Lv, Z.H., Zhang, H., Tang, Y., Liu, Y.L., Zhang, X., 2018. Petrogenesis of syn-orogenic rare metal pegmatites in the Chinese Altai: Evidences from geology, mineralogy, zircon U-Pb age and Hf isotope. Ore Geol. Rev. 95, 161–181.

Lv, Z.H., Chen, J., Zhang, H., Tang, Y., 2021a. Petrogenesis of Neoproterozoic rare metal granite-pegmatite suite in JiangnanOrogen and its implications for rare metal mineralization of peraluminous rock in South China. Ore Geol. Rev. 128, 103923.

Lv, Z.H., Zhang, H., Tang, Y., 2021b. Anatexis origin of rare metal/earth pegmatites: Evidences from the Permian pegmatites from the Permian pegmatites Chinese Altai. Lithos 380–381, 105865.

Ma, T.Q., Chen, L.X., Bai, D.Y., Zhou, K.J., Li, G., Wang, X.H., 2009. Zircon SHRIMP dating and geochemical characteristics of Neoproterozoic granites in southeastern Hunan. Geol. China 36, 65–73 in Chinese with English abstract.

Mao, J.R., Li, Z.L., Ye, H.M., 2014. Mesozoic tectono-magmatic activities in South China: Retrospect and prospect. Sci. China: Earth Sci. 57, 2853–2877 in Chinese with English abstract.

McCauley, A., Bradley, D.C., 2014. The global age distribution of granitic pegmatites. Can. Mineral. 183–190.

Mezger, K., Hanson, G.N., Bohlen, S.R., 1989. U-Pb Systematics of garnet: Dating the growth of Garnet in the Late ArcheanPikwitonei Granulite Domain at Cauchon and Natawahunan Lakes, Manitoba, Canada. Contrib. Miner. Petrol. 101, 136–148.

Müller, A., Romer, R.L., Pedersen, R.B., 2017. The Sveconorwegian Pegmatite Province-Thousands of pegmatites without parental granites. Can. Mineral. 55, 283–315.

Nasdala, L., Zhang, M., Kempe, U., Panczer, G., Pltze, M., 2003. Spectroscopic methods applied to zircon. Rev. Mineral. Geochem. 53, 427–467.

Pandur, K., Ansdell, K.M., Eglington, B.M., Harper, C.T., Hanchar, J.M., McFarlane, C.R.M., 2020. In situ U-Pb geochronology, Lu-Hf and Sm-Nd isotope systematics of the Hoidas Lake REE deposit, northern Saskatchewan, Canada. Precamb. Res. 339, 105591.

Pearce, J.A., Kempton, P.D., Nowell, G.M., Noble, S.R., 1999. Hf–Nd element isotope perspective on the nature and provenance of mantle and subduction components in Western Pacific arc-basin systems. J. Petrol. 40, 1579–1611.

Pin, C., Paquette, J.L., 1997. A mantle-derived bimodal suite in the Hercynian belt: Nd isotope and trace element evidence for a subduction-related rift origin of the late Devonian Brevenne metavolcanics, Massif Central (France). Contrib. Mineral. Petrol. 129, 222–238.

Roda-Robles, E., Villaseca, C., Pesquera, A., Gil-Crespo, P.P., Vieira, R., Lima, A., Olave, I., 2018. Petrogenetic relationships between Variscangranitoids and Li-(F-P)-rich aplite-pegmatites in the Central Iberian Zone: Geological and geochemical constraints and implications for other regions from the European Variscides. Ore Geol. Rev. 95, 408–430.

Rollinson, H.R., Windley, B.F., 1980. Selective elemental depletion during metamorphism of Archean granulites. Contrib. Mineral Petrol. 72, 257–263.

Schärer, U., 1984. The effect of initial ^{230}Th disequilibrium on young U-Pb ages: the Makalucase, Himalaya. Earth Planet. Sci. Lett. 67, 191–204.

Scherer, E., Munker, C., Mezger, K., 2001. Calibration of the lutetium hafnium clock. Science (New York, N.Y.) 293, 683–687.

Sevigny, J.H., Hanson, G.N., 1992. U-Pb dating of garnets in Paleozoic leucogranites, southwestern New England Appalachians. Can. J. Anaesth. 51, 638.

Shan, L., Ke, X.Z., Pang, Y.C., Liu, J.J., Zhao, X.M., Wang, J., Kang, B., Zhang, K., 2017. Zircon LA-ICP-MS U-Pb chronology, Lu-Hf characteristics and its geological significance of the Neoproterozoic magma activity in Lishan area from the northestern Hunan Province. Geol. Sci. Tech. Infor. 36, 32–42 in Chinese with English abstract.

Shearer, C.K., Papike, J.J., Jolliff, B.L., 1992. Petrogenetic links among granites and pegmatites in the Harney Peak rare-element granite-pegmatite system, Black Hills, South Dakota. Can. Mineral. 30, 785–809.

Shu, L., Zhou, G., Shi, Y., Yin, J., 1994. Study of the high pressure metamorphic blueschist and its late Proterozoic age in the eastern Jiangnan belt. Chin. Sci. Bull. 39, 1200–1204.

Shu, L.S., Zhou, X.M., 2002. Late Mesozoic tectonism of Southeast China. Geol. Rev. 48, 249–260 in Chinese with English abstract.

Shu, L.S., Zhu, W.B., Xu, Z.Q., 2021. Geological settings and metallogenetic conditions of the granite-type lithium ore deposits in South China. Acta Geol. Sin. 95, 3099–3114.

Soderlund, U., Patchett, P.J., Vervoort, J.D., Isachsen, C.E., 2004. The ^{176}Lu decay constant determined by Lu-Hf and U-Pb isotope systematics of Precambrian mafic intrusions. Earth Planet. Sc. Lett. 219, 311–324.

Sun, W.D., Yang, X.Y., Fan, W.M., Wu, F.Y., 2012. Mesozoic large scale magmatism and mineralization in South China: Preface. Lithos 150, 1–5.

Suzuki, K., Shimizu, H., Masuda, A., 1996. Re-Os dating of molybdenites from ore deposits in Japan: implication for the closure temperature of the Re-Os system for molybdenite and the cooling history of molybdenum ore deposits. Geochim. Cosmochim. Acta 60 (16), 3151–3159.

Tang, Y., Chen, H., Dong, C., Yang, S.F., Shen, Z.Y., Chen, X.G., Fu, L.L., 2013. Middle triassic post-orogenic extension on Hainan Island: Chronology and geochemistry constraints of bimodal intrusive rocks. Sci. China Earth Sci. 56, 783–793.

Tang, Y., Zhao, J.Y., Zhang, H., Cai, D.W., Lv, Z.H., Liu, Y.L., Zhang, X., 2017. Precise columbite-(Fe) and zircon U-Pb dating of the Nanping No. 31 pegmatite vein in northeastern Cathaysia Block, SE China. Ore Geol. Rev. 83, 300–311.

Tkachev, A.V., 2011. Evolution of metallogeny of granitic pegmatites associated with orogens throughout geological time. Geol. Soc. Lond. Spec. Publ. 350, 7–23.

Tomascak, P.B., Krogstad, E.J., Walker, R.J., 1996. U-Pb monazite geochronology of granitic rocks from Maine: implications for late Paleozoic tectonics in the Northern Appalachians. J. Geol. 104, 185–195.

Vervoort, J.D., Patchett, P.J., Blichert-Toft, J., Albarède, F., 1999. Relationships between Lu-Hf and Sm-Nd isotopic systems in the global sedimentary system. Earth Planet. Sc. Lett. 168, 79–99.

Wang, Z., Chen, Z.Y., Li, J.K., Xiong, X., Yang, H., Zhou, F.C., 2019. Indication of mica minerals for magmatic-hydrothermal evolution of Renli rare metal pegmatite deposit. Miner. Depos. 38, 1039–1814 in Chinese with English abstract.

Wang, L.X., Ma, C.Q., Zhang, C., Zhang, J.Y., Marks, M.A.W., 2014a. Genesis of leucogranite by prolonged fractional crystallization: A case study of the Mufushan complex, South China. Lithos 206–207, 147–163.

Wang, D., Shu, L., 2012. Late Mesozoic basin and range tectonics and related magmatism in southeast China. Geosci. Front. 3, 109–124 in Chinese with English abstract.

Wang, Z.L., Xu, D.R., Chi, G.X., Shao, Y.J., Lai, J.Q., Deng, T., Guo, F., Wang, Z., Dong, G.J., Ning, J.T., Zou, S.H., 2017b. Mineralogical and isotopic constraints on the genesis of the Jingchong Co-Cu polymetallic ore deposit in northeastern Hunan Province, South China. Ore Geol. Rev. 88, 638–654.

Wang, D.Z., Zhou, X.M., 2002. Genesis of Late Mesozoic Volcanic-Intrusive Complex of Southeast China and Crustal Evolution. Science Press, Beijing, pp. 1–295 in Chinese.

Wang, X., Zhou, J., Qiu, J., Zhang, W., Liu, X., Zhang, G., 2006. LA-ICP-MS U-Pb zircon geochronology of the Neoproterozoic igneous rocks from Northern Guangxi, South China: implications for tectonic evolution. Precamb. Res. 145, 111–130.

Wang, X.L., Zhou, J.C., Griffin, W.L., Zhao, G.C., Yu, J.H., Qiu, J.S., Zhang, Y.J., Xing, G.F., 2014b. Geochemical zonation across a Neoproterozoicorogenic belt: Isotopic evidence from granitoids and metasedimentary rocks of the Jiangnan orogeny, China. Precamb. Res. 242, 154–171.

Wang, X.L., Zhou, J.C., Chen, X., Zhang, F.F., Sun, Z.M., 2017a. Formation and evolution of the JinagnanOrogen. Bull. Mineral. Petrol. Geochem. 36, 714–734 in Chinese with English abstract.

Wei, J.Q., Zhu, D., Wang, F., Li, J., Lu, L., Pan, S.X., 2021. Mineralogical chcracteristics and occurrence state of niobium and tantalum in the Duanfengshan Nb-Ta deposit in Hubei Province, China. Acta Mineral. Sin. 41, 319–326 in Chinese with English abstract.

Wen, C.H., Shao, Y.J., Xiong, Y.Q., Li, J.K., Jiang, S.Y., 2021. Ore genesis of the Baishawo Be-Li-Nb-Ta deposit in the northeast Hunan Province, south China: Evidence from geological, geochemical, and U-Pb and Re-Os geochronologic data. Ore Geol. Rev. 129, 103895.

Wiedenbeck, M., Alle, P., Corfu, F., Griffin, W.L., Meier, M., Oberli, F., Vonquadt, A., Roddick, J.C., Speigel, W., 1995. Three natural zircon standards for U-Th–Pb, Lu–Hf, trace element and REE analyses. Geostandard. Newslett. 19, 1–23.

Williams, I.S., Hergt, J.M., 2000. U–Pb dating of Tasmanian dolerites: a cautionary tale of SHRIMP analysis of high-U zircon. in: Woodhead, J.D., Hergt, J.M., Noble, W.P. (Eds.), Beyond 2000: New Frontiers in Isotope Geoscience: Lorne, pp. 185–188.

Wu, F.Y., Yang, Y.H., Xie, L.W., Yang, J.H., Xu, P., 2006a. Hf isotopic compositions of the standard zircons and baddeleyites used in U-Pb geochronology. Chem. Geol. 234, 105–126.

Wu, R.X., Zheng, Y.F., Wu, Y.B., Zhao, Z.F., Zhang, S.B., Liu, X.M., Wu, F.Y., 2006b. Reworking of juvenile crust: element and isotope evidence from neoproterozoicgranodiorite in south China. Precam. Res. 146, 179–212.

Xiong, Y.Q., Jiang, S.Y., Wen, C.H., Yu, H.Y., 2020. Granite-pegmatite connection and mineralization age of the giant Renli Ta-Nb deposit in South China: Constraints from U-Th-Pb geochronology of coltan, monazite, and zircon. Lithos 358–359, 05422.

Xu, D., Deng, T., Dong, G., Ning, J., Wang, Z., Zhang, J., Zou, F., Zhou, Y., Chen, G., Yu, D., Ye, T., 2017. Zircon U-Pbgeochronological and geochemical characteristics of the Lianyunshan two-mica monzogranites in northeastern Hunan province: implications for petrogenesis and tectonic setting associated with polymetallic mineralization. Earth Sci. Front. 24, 104–122 in Chinese with English abstract.

Xu, D.R., Deng, T., Chi, G.X., Wang, Z.L., Zou, F.H., Zhang, J.L., Zou, S.H., 2019b. Gold mineralization in the JiangnanOrogenic Belt of South China: Geological, geochemical and geochronological characteristics, ore deposit-type and geodynamic setting. Ore Geol. Rev. 88, 565–618.

Xu, C., Li, J.K., Shi, G.H., Li, P., Liu, X., Zhang, L.P., 2019a. Zircon U-Pb age and Hf isotopic composition of porphyaceous biotite granite in south margin of Mufushan and their geological implications. Miner. Depos. 38 (5), 1053–1068 in Chinese with English abstract.

Yan, Q.H., Wang, H., Chi, G.X., Wang, Q., Hu, H., Zhou, K.L., Zhang, X.Y., 2022. Reconnition of a 600-km-long late Triassic rare metal (Li-Rb-Be-Nb-Ta) pegmatite belt in the Western Kunlun orogenic belt, western China. Econ. Geol. 117 (1), 213–236.

Yang, H., Chen, Z.Y., Li, J.K., Li, P., Xiong, X., Wang, Z., Zhou, F.C., 2019. Relation between the mineralization and evolution of mica and feldspar components of Renli-Chuangziyuan No. 5 pegmatite, northeast Hunan. Miner. Depos. 38, 851–866 in Chinese with English abstract.

Yang, Y.H., Wu, F.Y., Yang, J.H., Chew, D.M., Xie, L.W., Chu, Z.Y., Huang, C., 2014. Sr and Nd isotopic compositions of apatite reference materials used in U-Th–Pb geochronology. Chem. Geol. 385, 35–55.

Yang, X., Zhang, Y.Z., Cui, X., Yu, P.P., Xu, W.J., 2020. Geochemistry and detrital zircon U-Pb ages of sedimentary rocks from NeoproterozoicLengjiaxi group in NE Hunan Province. Earth Sci. 45, 3461–3474 in Chinese with English abstract.

Yao, J., Shu, L., Santosh, M., 2014. Neoproterozoic arc–trench system and breakup of the South China Craton: constraints from N-MORB type and arc-related mafic rocks, and anorogenic granite in the Jiangnanorogenic belt. Precamb. Res. 247, 187–207.

Ying, Y., Chen, W., Lu, J., Jiang, S., Yang, Y., 2017. In situ U-Th–Pb ages of the Miaoyacarbonatite complex in the South Qinlingorogenic belt, Central China. Lithos 290–291, 159–171.

Yu, D.S., Xu, D.R., Wang, Z.L., Xu, K., Huang, Q.Y., Zou, S.H., Zhao, Z.X., Deng, T., 2021. Trace element geochemistry and O-S-Pb-He-Ar isotopic systematics of the LishanPb-Zn-Cu hydrothermal deposit, NE Hunan, South China. Ore Geol. Rev. 133, 104091.

Zhang, R., Lu, J., Lehmann, B., Li, C., Li, G., Zhang, L., Guo, J., Sun, W., 2017. Combined zircon and cassiterite U-Pb dating of the Piaotang granite-related tungsten–tin deposit, southern Jiangxi tungsten district, China. Ore Geol. Rev. 82, 268–284.

Zhang, H., Lv, Z.H., Tang, Y., 2019. Metallogeny and prospecting model as well as propecting direction of pegmatite-type rare metal ore deposits in Altay orogenic belt, Xinjiang. Miner. Depos. 38, 792–814 in Chinese with English abstract.

Zhao, K., Jiang, S., Ling, H., Palmer, M.R., 2014. Reliability of LA-ICP-MS U-Pb dating of zircons with high U concentrations: a case study from the U-bearing Douzhashan Granite in South China. Chem. Geol. 389, 110–121.

Zhao, J.H., Zhou, M.F., Yan, D.P., Zheng, J.P., Li, J.W., 2011. Reappraisal of the ages of Neoproterozoic strata in South China: no connection with the Grenvillian orogeny. Geology 39, 299–302.

Zheng, Y.F., Zhang, S.B., Zhao, Z.F., Wu, Y.B., Li, X.H., Li, Z.X., Wu, F.Y., 2007. Contrasting zircon Hf and O isotopes in the two episodes of Neoproterozoicgranitoids in South China: implications for growth and reworking of continental crust. Lithos 96, 127–150.

Zhou, F.C., Li, J.K., Liu, X., Li, P., Huang, Z.B., Shi, W.K., Su, J.N., Chen, H., Huang, X.Q., 2019a. Geochemical characteristics and genetic significance of orebodies in Renli Nb-Ta deposit, Hunan Province. Acta Geol. Sin. 93, 1392–1404 in Chinese with English abstract.

Zhou, F.C., Liu, X., Li, J.K., Huang, Z.B., Xiao, G.Q., Li, P., Zhou, H.X., Shi, W.K., Tan, L.M., Su, J.N., Chen, H., Wang, X.M., 2019b. Metallogenic characteristics and propecting direction of Renli super-large rere metal deposit in Hunan Province, China. Geotec. Metal. 43, 77–91 in Chinese with English abstract.

Zhou, F.C., Huang, Z.B., Liu, X., Su, J.N., Huang, X.Q., Wang, Z., Chen, H., Zhang, Z.D., Nuo, X.R., Li, J.B., Li, Z.H., Zhang, L.P., Zeng, L., Li, X.M., 2020. Re-Os dating of molybdenite from the RenliNb-Ta Deposit, Hunan Peovince, and its geological significance. Geotec. Metal. 44, 476–485 in Chinese with English abstract.

Zhou, X.M., Sun, T., Shen, W.Z., Shu, L.S., Niu, Y.L., 2006. Petrogenesis of Mesozoic granitoids and volcanicrocks in South China: A response to tectonicevolution. Episodes: English edition 29, 26–33.

Zhou, J.C., Wang, X.L., Qiu, J.S., 2009. Geochronology of Neoproterozoic mafic rocks and sandstones from northeastern Guizhou, South China: coeval arc magmatism and sedimentation. Precamb. Res. 170, 27–42.

Zou, S.H., Zou, F.H., Ning, J.T., Deng, T., Yu, D.S., Ye, T.W., Xu, D.R., Wang, Z.L., 2018. A. stand-alone Co mineral deposit in northeastern Hunan Province, South China: Its timing, origin of ore fluids and metal Co, and geodynamic setting. Ore Geol. Rev. 92, 42–60.

Further reading

Dill, H.G., 2018. Geology and chemistry of Variscan-type pegmatite systems (SE Germany) with special reference to structural and chemical pattern recognition of felsic mobile components in the crust. Ore Geol. Rev. 92, 205–239.

Schärer, U., Corfu, F., Demaiffe, D., 1997. U-Pb and Lu–Hf isotopes in baddeleyite and zircon megacrysts from the Mbuji-Mayikimberlite: constraints on the subcontinental mantle. Chem. Geol. 143, 1–16.